NUMERICAL IMPLEMENTATION OF PLASTIC-DAMAGE MODEL FOR CONCRETE UNDER CYCLIC LOADING: APPLICATION TO CONCRETE DAMS

by

Jeeho Lee
Gregory L. Fenves

Report to U.S. Bureau of Reclamation
for Research Sponsored under
Grant No. 1425-2-FC-81-00380

Report No. UCB/SEMM-94/03
Structural Engineering, Mechanics and Materials
Department of Civil Engineering
University of California at Berkeley
Berkeley, California

May 1994

ABSTRACT

Modeling material softening as well as hardening behavior is important in the analysis of concrete structures, such as dams. The plastic-damage model consists of constitutive relations for simulating the softening behavior under tensile and high-compressive loading and the hardening behavior under low-compressive loading. An advantage of using the plastic-damage model is that both microcracking, which is known to cause the softening, and hardening can be represented by equivalent inelastic strain. This approach provides a simple and powerful method when solving the problem subjected to combined tensile and compressive loading. Lubliner's plastic-damage model gives many features needed in simulating concrete materials. The model uses a damage variable to represent both hardening and softening damage. Degradation of elastic secant stiffness is also available in the model.

A numerical model, which is based on the modified version of the Lubliner plastic-damage model, is developed to simulate concrete behavior under cyclic loading. First, the evolution equation of cohesion and the degradation rule of elastic stiffness of the Lubliner's model are simplified. A new return-map algorithm, which is called *the spectral return-map algorithm*, is introduced to solve the constitutive model numerically. In the new algorithm, the return-map equations are decoupled by the spectral decomposition. These decoupled equations are iterated until all governing nonlinear constitutive relations are satisfied. The principal values of stresses and plastic strains play an important role in plastic-damage models, such as Lubliner's. By using the spectral return-map algorithm, it is not necessary to calculate these principal values repeatedly in an iteration for the stress computation. The plane stress version of the spectral return-map algorithm is directly derived from the general formulation.

The plane stress formulation of the algorithm is implemented as one part of the existing nonlinear finite element program, FEAP. The numerical examples for monotonic and cyclic loading cases have been tested. The numerical results agree well with the corresponding experimental results. The model shows promise for application to the earthquake analysis and evaluation of concrete dams.

TABLE OF CONTENTS

Chapter 1

INTRODUCTION

1.1 Background

The earthquake analysis and evaluation of concrete dams is well–established using linear models of concrete behavior. Extensive research, however, has shown that a linear model does not adequately represent the performance of concrete dams since tensile cracks are expected to form and propagate during a design level earthquake. The questions that must be answered in a dam safety evaluation are whether cracks will form, how will they propagate, what is the damage, and will the dam remain stable during and after an earthquake. The motivation for this research is to develop a fundamentally sound, yet practical, model of mass concrete appropriate for use in nonlinear, dynamic earthquake analysis of dams.

There have been many attempts to model crack propagation and failure in concrete structures. In contrast to other materials such as metal and glass, linear elastic fracture mechanics (LEFM) has not been successfully applied to simulating concrete cracking.

There are three major approaches in modeling concrete microcracks. One is called as the discrete crack model, which assumes a crack as a geometrical discontinuity [Hillerborg, et al., 1976; Du, et al., 1990; Ayari and Saouma, 1990; Martha, et al., 1992]. The discrete crack model has clear physical concepts, and gives good results for the stationary crack problem. It has been shown, however, that numerical methods based on the discrete crack model are inefficient and give relatively poor accuracy for the crack propagation problem [Rots, 1988; Yamaguchi and Chen, 1990].

Another approach, the so-called smeared crack model, assumes a cracked solid to be a continuum. This model was introduced by Rashid [Rashid, 1968] and later modified by Bazant and Oh [Bazant and Oh, 1983 and 1984] and other investigators [Yamaguchi and Chen, 1990; Dahlblom and Ottosen, 1990; Gajer and Dux, 1990]. In this model, crack initiation and propagation are represented only in terms of changing material properties. The smeared crack model is much simpler to implement, because there is no free surface and change of the topology during crack propagation. Though the smeared crack model is convenient when numerically implemented, many problems have been found [Rots, 1988]:

1) There is the dependency of analysis with respect to crack directions.
2) It uses an arbitrarily-defined shear retention factor.

3) It is hard to define stress paths at cracked points for cyclic-loading and unloading.
4) It is difficult to model cracking with other inelastic phenomena at damaged area.

A third approach, the plasticity-based crack model [Ju, 1989; Lubliner, et al., 1989; Pramono and William, 1989; Yazdani and Schreyer, 1990], is not as popular as the smeared crack model, but is more powerful for modeling the complicated behavior of concrete materials. The model represents cracked solid body not by direct description, but by using equivalent continuum strains. In this approach, the crack propagation is assumed to be a limit state of plastic yielding so that inelastic behavior, including the crack propagation, are represented in a consistent constitutive model.

Among several versions of the plasticity-based model, the plastic-damage model [Lubliner, et al., 1989; Oller, et al., 1990] is a good approach to simulate mass concrete behavior, because the model includes the damage properties which are observed in brittle materials. In this model, the microcracks in concrete are represented by increasing values of damage variables which decrease the size of a yield surface and/or degrade a secant stiffness. Another important feature of the plastic-damage model is that it can model the compressive yielding and softening as well as the tensile failure in one constitutive relation. Consequently, the plastic-damage approach provides an opportunity to model a wide range of nonlinear elastic and inelastic behavior of concrete.

1.2 Objectives and Overview

There are two principal objectives in this study. The first objective is to review and modify the original plastic-damage model, which was suggested by Lubliner [Lubliner, et al., 1989], to be suitable for the numerical model that is designed mainly for cyclic loading problems. Developing a numerical model for cyclic loading problems can be justified as the preliminary step in considering dynamic problems. The cohesion evolution of a yield function and the degradation of elastic secant stiffness are simplified for this purpose. The proposed tangent stiffness in the original model is not appropriate for the return-map algorithm which has been known to be the most efficient and powerful numerical method for elastoplastic problems. The consistent algorithmic tangent stiffness, which is necessary to maintain good convergence rate in solving nonlinear structural problems associated with the elastoplastic constitutive model [Simo and Tayor, 1985 and 1986; Simo, et al., 1988], are derived in place of the continuous tangent stiffness. The algorithmic tangent stiffness is related to the numerical model rather than the constitutive model itself.

The second objective is to develop an accurate and efficient numerical algorithm for the improved model. Developing numerical algorithms for the governing equations of a constitutive model is an important topic in addition to deriving the equations themselves, because many numerical difficulties, such as convergence and existence, may occur. The most important numerical procedure in solving elastoplastic problems is the computation of stresses at each loading step. It is critical to evaluate stresses accurately, because accumulated errors in the computed stresses increase rapidly causing divergence of solution. The plastic-damage model has many terms of principal values of stress and plastic strain. The numerical algorithm must perform these calculations, which would be performed repeatedly during iteration for the solution, in an efficient way. The existing return-map algorithms are not appropriate to treat this kind of constitutive model. Furthermore, the plane stress formulation is more complicated than the general three-dimensional and the plane strain problems because constraints are imposed on the stress, which is the main unknown in the finite element method. Consequently, the numerical model should be able to simulate the modified constitutive model efficiently for the plain stress problem as well as the three-dimensional problem. In the present study, a new version of the return-map algorithm is introduced to resolve the problems described so far. A spectral decoupling technique is applied to the standard return-map algorithm to derive the new algorithm, which is called *the spectral return-map algorithm* in the study.

The constitutive model is described in Chapter 2. The rate-independent plasticity and the plastic-damage model are also reviewed in this chapter. Chapter 3 presents the numerical implementation for the model. The numerical algorithm to solve nonlinear differential equations, describing in Chapter 2, is derived for the general problems and more specifically for the plane stress problems. Finally, test results using the numerical algorithm are presented with the experimental results in Chapter 4.

This page is left blank

Chapter 2

CONSTITUTIVE MODEL

2.1 Introduction

The present constitutive model is based on the plastic-damage model which was suggested by Lubliner [Lubliner, et al., 1989]. The original plastic-damage model is modified for simulating concrete behavior under cyclic loads. Basically, the rate-independent plasticity theory and the infinitesimal deformation theory are applied to the elastic and inelastic constitutive law in the model.

One of the most important aspect of concrete behavior is the strain softening. The softening zone is known to result from the formation of microcracks. A constitutive model for concrete materials should represent the softening behavior correctly, as well as the hardening behavior which occurs under compressive loading. A damage variable is used to model both softening and hardening in Lubliner's model. In addition to the damage variable, the model introduces elastic and plastic degradation variables to simulate the degradation of elastic tangent which is known to be very significant in concrete. In the present model, the concept of the damage variable is used as in Lubliner's model. The degradation model is slightly modified from the original one. The elastic degradation is directly related to the total strain to simulate the crack opening/closing under cyclic loading. To avoid singularities arising from the corners of the yield surface and to use a non-associative flow rule as well, a multi-potential flow rule is introduced.

The system of the rate equations modeling softening behavior of materials are ill-posed ordinary differential equations [Borst and et al., 1993]. Consequently, the uniqueness of solution is not guaranteed. In this study, the existence of solution is assumed and the converged solution is accepted as the real solution because the proofs of these conditions are beyond the scope of the study. One source of the ill-posedness is the mesh-sensitivity in the context of the finite element method. The characteristic length concept [Oliver, 1989] is used here. The ill-posedness of the problem has been discussed with the stability of the structural boundary problem [Borst and et al., 1993].

This chapter consists of three parts. The first part describes the fundamental constitutive rules of the model. The second and the third parts present the damage model, which is related to the elastic and plastic strain. The tensor notation is used throughout this chapter.

2.2 Rate-Independent Plasticity

2.2.1 Stress-Strain Relations

In the incremental theory of plasticity, the strain is assumed to be decomposed into the elastic part and the plastic part:

$$\boldsymbol{\varepsilon} = \boldsymbol{\varepsilon}^e + \boldsymbol{\varepsilon}^p \tag{2.2.1}$$

For the linear hyper-elastic materials, the elastic strain is the recoverable portion in the total strain, which is given by:

$$\boldsymbol{\varepsilon}^e = \mathbf{D}^{-1} : \boldsymbol{\sigma} \tag{2.2.2}$$

From Eq. 2.2.1 and Eq. 2.2.2, the plastic strain becomes:

$$\boldsymbol{\varepsilon}^p = \boldsymbol{\varepsilon} - \mathbf{D}^{-1} : \boldsymbol{\sigma} \tag{2.2.3}$$

where $\mathbf{D}$ is the elastic secant stiffness which is a function of time. Since rate-independent plasticity is assumed, the stress-strain relation can be written as:

$$\boldsymbol{\sigma} = \mathbf{D} : (\boldsymbol{\varepsilon} - \boldsymbol{\varepsilon}^p) \tag{2.2.4}$$

The total strain can be split into the deviatoric part and the spherical part:

$$\boldsymbol{\varepsilon} = \mathbf{e} + \frac{\theta}{3}\mathbf{I} \tag{2.2.5}$$

where $\theta = \varepsilon_{kk}$ and $\mathbf{e}$ is the deviatoric strain.

Assuming the strain decomposition, such as Eq. 2.2.1, the split strains become:

$$\mathbf{e} = \mathbf{e}^e + \mathbf{e}^p \tag{2.2.6a}$$

$$\theta = \theta^e + \theta^p \tag{2.2.6b}$$

The stress-strain relation for the homogeneous isotropic material is expressed in the form:

$$\boldsymbol{\sigma} = 2\mu(\mathbf{e} - \mathbf{e}^p) + \lambda(\theta - \theta^p)\mathbf{I} \tag{2.2.7}$$

where μ and λ are the Lame' constants. Eq. 2.2.7 can be used in the plane strain case simply by condensing the stress and strain tensors. On the other hand, in the plane stress case, Eq. 2.2.7 should be modified, because the constraint is imposed to the stress. Replacing λ with $2\lambda G/(\lambda + 2G)$, where G is the elastic shear modulus, in Eq. 2.2.7 gives the stress-strain relation for the plane stress problems:

$$\begin{aligned} \boldsymbol{\sigma} &= 2\mu\boldsymbol{\varepsilon}^e + \frac{2\lambda G}{\lambda + 2G}\theta^e\mathbf{I} \\ &= 2G(\boldsymbol{\varepsilon} - \boldsymbol{\varepsilon}^p) + \frac{\nu E}{1-\nu^2}(\theta - \theta^p)\mathbf{I} \end{aligned} \tag{2.2.8}$$

θ^e in Eq. 2.2.8 is not the same as that in Eq. 2.2.7, but is equal to the sum of the diagonal entries of the 2-dimensional stress tensor (that is, $\theta^e = \varepsilon_{11}^e + \varepsilon_{22}^e$).

2.2.2 Yield Surface

The yield criterion for frictional materials like concrete and rock can be written in the form:

$$F(\boldsymbol{\sigma}) = c \tag{2.2.9}$$

where c is the cohesion.

The Mohr-Coulomb and the Drucker-Prager criteria are the most well-known forms of yield functions. The yield function, F, is a scalar function of invariants of the stress tensors. In order to make a yield surface more realistic, the J_3 term as well as I_1 and J_2 is included in F [Chen and Han, 1988]. In Lubliner's model [Lubliner, et al., 1989], the algebraically largest principal stress is included instead of J_3. This term makes the yield function represent the two different behaviors in the tensile region and the compressive region more precisely. The yield function of Lubliner's model is:

$$F(\boldsymbol{\sigma}) = \frac{1}{1-\alpha}(\alpha I_1 + \sqrt{3J_2} + \beta\hat{\sigma}_{\max}) \tag{2.2.10}$$

where α and β are dimensionless constants and $\hat{\sigma}_{\max}$ is the maximum principal stress. The plane stress cross-section of the yield surface is given in Fig. 2.1. The parameters, α and β, determine the shape of the yield surface. These parameters are evaluated so that the yield function accurately represents the real experimental data. Three independent material strength data obtained in the plane stress condition can be used to determine the parameters.

The initial cohesion, c_0, can be obtained by assuming the uniaxial compressive loading state:

$$c_0 = f_{cy} \tag{2.2.11}$$

where f_{cy} is the uniaxial initial yielding compressive stress.

From the uniaxial initial yielding compressive stress and the biaxial initial yielding compressive stress f'_{by},

$$\alpha = \frac{f_{by} - f_{cy}}{2f_{by} - f_{cy}} \qquad 0 \le \alpha < 1 \tag{2.2.12}$$

Finally, the uniaxial initial yielding tensile stress f_{ty}, which is generally assumed to be the same as the maximum tensile strength, is used with f_{cy} to compute β:

$$\beta = \frac{f_{cy}}{f_{ty}}(\alpha - 1) - (\alpha + 1) \qquad 0 \le \beta < 1 \tag{2.2.13}$$

Note that the biaxial tensile strength depends on the others and is always a little less (about 1.3%) than the uniaxial tensile strength.

The gradient vector, **f,** is defined as:

$$\mathbf{f} = \frac{\partial}{\partial \boldsymbol{\sigma}} F(\boldsymbol{\sigma}) \tag{2.2.14}$$

Applying the chain rule to Eq. 2.2.14 gives

$$\frac{\partial F}{\partial \boldsymbol{\sigma}} = \frac{1}{1-\alpha}\left(\alpha \frac{\partial I_1}{\partial \boldsymbol{\sigma}} + \frac{3}{2\sqrt{3J_2}} \frac{\partial J_2}{\partial \boldsymbol{\sigma}} + \beta \frac{\partial \hat{\sigma}_{\max}}{\partial \boldsymbol{\sigma}}\right) \tag{2.2.15}$$

In the numerical implementation explained later, not $\frac{\partial F}{\partial \boldsymbol{\sigma}}$ but $\frac{\partial F}{\partial \hat{\boldsymbol{\sigma}}}$, where $\hat{\boldsymbol{\sigma}}$ is the principal stress, is used.

The Kuhn-Tucker conditions from the optimization theory give the loading/unloading condition which can be used in the strain-softening material as well as the work-hardening and the perfect-plastic materials. These represent the relations between the yield criterion and the plastic loading factor, $\dot{\lambda}$:

$$\mathfrak{I}(\boldsymbol{\sigma}, c) = F(\boldsymbol{\sigma}) - c \le 0 \tag{2.2.16a}$$

$$\dot{\lambda} \ge 0 \tag{2.2.16b}$$

$$\mathfrak{I}(\boldsymbol{\sigma}, c)\dot{\lambda} = 0 \tag{2.2.16c}$$

Note $\dot{\lambda}$ is not the time derivative of the Lame' constant. These conditions play an important role in the numerical implementation.

2.2.3 Flow Rule

The flow rule gives the relation between the plastic flow direction and the plastic strain rate. Generally the relation is:

$$\dot{\boldsymbol{\varepsilon}}^P = \dot{\lambda}\frac{\partial G}{\partial \boldsymbol{\sigma}} \tag{2.2.17}$$

where $\dot{\lambda}$ is the plastic loading factor and G is the plastic potential energy function. When the yield function F is chosen as the plastic potential energy function, Eq. 2.2.17 is called the associative flow rule. Otherwise it is called a non-associative flow rule. The important advantage of using the associative flow rule is that the elastoplastic tangent stiffness matrix becomes symmetric. However, applying the associative flow rule to friction materials, such as concrete, may result in the improper control of the dilatancy [Chen and Han, 1988].

Because the yield surface in Eq. 2.2.10 is a combined geometric shape from two significantly different Drucker-Prager type functions, a single elliptical function cannot represent the plastic potential function corresponding to the yield surface. In the present study, the concept of the multi-surface yield function [Simo, et al., 1988; Hofstetter, et al., 1993] is used for the plastic potential function. That is, the plastic strain is assumed to be generated from several (usually two) different potential functions, which are the same as yield functions in the multi-surface concept. However, in this study, two different potential functions are used to generate the deviatoric part and spherical part of the plastic strain, respectively. Both concepts are equivalent to each other. G_1, which gives the deviatoric part of the plastic strain, and G_2, which generates the spherical part are defined as:

$$G_1 = \sqrt{3J_2} \tag{2.2.18a}$$

$$G_2 = I_1 \tag{2.2.18b}$$

The rate of the plastic strain from two potentials is then,

$$\dot{\boldsymbol{\varepsilon}}^P = \sum_{i=1}^{2} \dot{\lambda}_i \frac{\partial G_i}{\partial \boldsymbol{\sigma}} \tag{2.2.19}$$

Note that Eq. 2.2.19 is equivalent to the combination of two different Drucker-Prager type functions. The dilatancy can be controlled by choosing an appropriate $\lambda_1 - \lambda_2$ relation. The plastic strain can be obtained by substituting Eq. 2.2.18 into Eq. 2.2.19:

$$\dot{\boldsymbol{\varepsilon}}^p = \dot{\lambda}_1 \tilde{\mathbf{g}} + \dot{\lambda}_2 \mathbf{I} \tag{2.2.20}$$

where,

$$\tilde{\mathbf{g}} = \frac{\partial G_1}{\partial \boldsymbol{\sigma}} = \frac{3}{2\sqrt{3J_2}} (\boldsymbol{\sigma} - \frac{I_1}{3}\mathbf{I}) \tag{2.2.21}$$

2.3 Plastic-Damage Model

The plastic-damage variable, κ, is obtained by the rate equation:

$$\dot{\kappa} = A(\hat{\boldsymbol{\sigma}}, \kappa)\dot{\varepsilon}^p_{\max} + B(\hat{\boldsymbol{\sigma}}, \kappa)\dot{\varepsilon}^p_{\min} \tag{2.3.1}$$

where,

$\dot{\varepsilon}^p_{\max}$: the algebraically maximum eigenvalue of $\dot{\boldsymbol{\varepsilon}}^p$

$\dot{\varepsilon}^p_{\min}$: the algebraically minimum eigenvalue of $\dot{\boldsymbol{\varepsilon}}^p$

$\hat{\boldsymbol{\sigma}}$: the principal stress.

The possible formulation of A and B is given by Lubliner [Lubliner, et al., 1989]:

$$A(\hat{\boldsymbol{\sigma}}, \kappa) = \frac{f_t(\kappa)}{g_t} r(\hat{\boldsymbol{\sigma}}) \tag{2.3.2a}$$

$$B(\hat{\boldsymbol{\sigma}}, \kappa) = \frac{f_c(\kappa)}{g_c} (1 - r(\hat{\boldsymbol{\sigma}})) \tag{2.3.2b}$$

where f_t, f_c are scalar curves of κ for tension and compression and g_t, g_c are the areas of the complete stress-plastic strain curves of tension and compression, respectively. g_t, g_c are the dissipated energy density during the whole process of microcracking and known to depend on the size of localization zone, which cannot be evaluated in usual constitutive relations. Consequently, these parameters cannot become material properties. To maintain the objectivity of the damage evolution (softening) to the localization zone size, the normalized specific fracture energy, which is a material property, is normalized by the characteristic length, l, which is the assumed localization zone size. This normalized specific fracture energy is used as g_t. There has been controversy on the counterpart of the fracture energy in compressive failure [Lubliner, et al., 1989]. In this study, both the fracture energy and its counterpart in compressive failure are assumed as material properties. f_t, f_c are defined as:

$$f_t(\kappa) = \frac{f_{ty}}{a_t}[(1+a_t)\sqrt{\phi_t(\kappa)} - \phi_t(\kappa)] \tag{2.3.3a}$$

$$f_c(\kappa) = \frac{f_{cy}}{a_c}[(1+a_c)\sqrt{\phi_c(\kappa)} - \phi_c(\kappa)] \tag{2.3.3b}$$

where,

$$\phi_t(\kappa) = 1 + a_t(2+a_t)\kappa$$
$$\phi_c(\kappa) = 1 + a_c(2+a_c)\kappa$$

f_{ty}, f_{cy} : the initial tensile and compressive yield stress, respectively

a_t, a_c: parameters deciding the shapes of the tensile and compressive curves.

f_t, f_c represent the uniaxial stress curves as the functions of the damage variable. If the parameter in Eq. 2.3.3 is less than one, the corresponding curve represents only softening. Otherwise, the curve gives hardening at initial stage and softening after the peak strength. Fig. 2.2 shows the curve shapes for the different parametric values.

In Eq. 2.3.2, $r(\hat{\boldsymbol{\sigma}})$ is a weight factor such that $0 \le r(\hat{\boldsymbol{\sigma}}) \le 1$ and it is defined as:

$$r(\hat{\boldsymbol{\sigma}}) = \frac{\sum_{i=1}^{3} \langle \hat{\sigma}_i \rangle}{\sum_{i=1}^{3} |\hat{\sigma}_i|} \tag{2.3.4}$$

Using $< x >= (|x| + x)/2$, Eq. 2.3.4 becomes:

$$\begin{aligned} r &= \frac{|\hat{\sigma}_1| + |\hat{\sigma}_2| + |\hat{\sigma}_3| + \hat{\sigma}_1 + \hat{\sigma}_2 + \hat{\sigma}_3}{2(|\hat{\sigma}_1| + |\hat{\sigma}_2| + |\hat{\sigma}_3|)} \\ &= \frac{1}{2} + \frac{I_1}{2(|\hat{\sigma}_1| + |\hat{\sigma}_2| + |\hat{\sigma}_3|)} \end{aligned} \tag{2.3.5}$$

The gradient vectors of A and B with respect to stress are needed to solve the rate equation, Eq. 2.3.1. These vectors can be obtained by the chain rule as:

$$\frac{\partial A}{\partial \hat{\boldsymbol{\sigma}}} = \frac{f_t(\kappa)}{g_t} \frac{\partial r}{\partial \hat{\boldsymbol{\sigma}}} \tag{2.3.6}$$

From Eq. 2.3.5, we have the derivatives:

$$\frac{\partial r}{\partial \hat{\sigma}_i} = \frac{1}{2}\left(\frac{\Sigma - I_1 sgn(\hat{\sigma}_i)}{\Sigma^2}\right) \qquad i = 1,2,3 \tag{2.3.7}$$

where,

$$\Sigma = \|\hat{\boldsymbol{\sigma}}\|_1 = \sum_{i=1}^{3} |\hat{\sigma}_i|$$

and,

$$sgn(x) = \begin{cases} +1 & , x > 0 \\ 0 & , x = 0 \\ -1 & , x < 0 \end{cases}$$

After getting $\partial A / \partial \hat{\boldsymbol{\sigma}}$, we can obtain:

$$\frac{\partial B}{\partial \hat{\boldsymbol{\sigma}}} = \frac{f_c(\kappa)}{f_t(\kappa)} \frac{g_t}{g_c} \left(\frac{\partial A}{\partial \hat{\boldsymbol{\sigma}}}\right) = -\frac{f_c'}{f_t'} \frac{g_t}{g_c} \left(\frac{\partial A}{\partial \hat{\boldsymbol{\sigma}}}\right) \tag{2.3.8}$$

Because A and B are functions of κ as well as $\hat{\boldsymbol{\sigma}}$, the following are also given:

$$\frac{\partial A}{\partial \kappa} = \frac{\partial f_t(\kappa)}{\partial \kappa} \frac{r(\hat{\boldsymbol{\sigma}})}{g_t} \tag{2.3.9}$$

and

$$\frac{\partial B}{\partial \kappa} = \frac{\partial f_c(\kappa)}{\partial \kappa} \frac{(1 - r(\hat{\boldsymbol{\sigma}}))}{g_c} \tag{2.3.10}$$

The cohesion, c, in the yield function is determined by the plastic-damage variable, κ, and the principal stress, $\hat{\boldsymbol{\sigma}}$. Unless the tensile and the compressive stress-strain curves are assumed to be similar, the evolution of the cohesion variable should be expressed in a rate equation. A simple form of the rate equation is given by:

$$\dot{c} = r(\hat{\boldsymbol{\sigma}}) \dot{c}_t(\kappa) + (1 - r(\hat{\boldsymbol{\sigma}})) \dot{c}_c(\kappa) \tag{2.3.11}$$

where c_t and c_c are representing cohesion evolution in uniaxial tensile and compressive loading and are defined as:

$$c_t = -\frac{f_{cy}}{f_{ty}} f_t(\kappa) \tag{2.3.12a}$$

$$c_c = -f_c(\kappa) \tag{2.3.12b}$$

The derivatives of c_t and c_c are also given by:

$$\frac{dc_t}{d\kappa} = -\frac{f_{cy}}{f_{ty}}\frac{df_t(\kappa)}{d\kappa} \tag{2.3.13a}$$

$$\frac{dc_c}{d\kappa} = -\frac{df_c(\kappa)}{d\kappa} \tag{2.3.13b}$$

2.4 Stiffness Degradation

From experimental tests of concrete, it is clear that the degradation of stiffness occurs and becomes more significant as the strain increases. This phenomenon is known to be caused by microcracking. Under cyclic loading, mechanism of the stiffness degradation becomes more complicated because opening and closing of microcracks are involved.

The degradation of the elastic stiffness $\mathbf{D}(t)$ is assumed to depend on two sets of internal variables. The first set is the elastic degradation variables and the other is the plastic degradation variables. For simplicity, scalar degradation variables are used for both the elastic and the plastic degradation in this study. Consequently, the secant stiffness can be written in the form:

$$\mathbf{D}(t) = \mathbf{D}(d_e(t), d_p(t)) \tag{2.4.1}$$

where d_e is the elastic degradation variable and d_p is the plastic degradation variable and t is time. One simple form of Eq. 2.4.1, which is used in this study, is

$$\begin{aligned}\mathbf{D}(t) &= (1-d)\mathbf{D}_0 \\ &= (1-d_e(t))(1-d_p(t))\mathbf{D}_0\end{aligned} \tag{2.4.2}$$

where $\mathbf{D}_0$ is the initial elastic stiffness and d is the total degradation.

The elastic degradation should be defined differently in concrete because the stiffness change of concrete depends on crack-closing and opening, which are modeled by strains in the continuum damage model. Hence, it is reasonable that the elastic degradation is a

function of the total strain. Assuming the elastic degradation depends only on the absolute value of the algebraically largest principal strain $\hat{\varepsilon}_{\max}$, we can define:

$$d_e = 1 - \frac{\ln[1 + h < \hat{\varepsilon}_{\max} >]}{h < \hat{\varepsilon}_{\max} >} \tag{2.4.3}$$

where h is a parameter which controls the level of the elastic degradation. One possible method to decide h is calibration with an uniaxial stress state. Accordingly, the parameter becomes:

$$h = \frac{d_u}{(d_u - 1)v\varepsilon_u} \tag{2.4.4}$$

where ε_u is the uniaxial compressive strain at which the degradation of an elastic tangential stiffness becomes d_u.

The derivative of the elastic degradation variable with respect to strain is given by

$$\frac{\partial d_e}{\partial \boldsymbol{\varepsilon}} = \frac{\mathrm{H}(\hat{\varepsilon}_{\max})}{h < \hat{\varepsilon}_{\max} >^2} \{\ln[1 + h < \hat{\varepsilon}_{\max} >] - < \hat{\varepsilon}_{\max} > \frac{h}{1 + h < \hat{\varepsilon}_{\max} >}\} \frac{\partial \hat{\varepsilon}_{\max}}{\partial \boldsymbol{\varepsilon}} \tag{2.4.5}$$

where H is the Heaviside step function.

The plastic degradation is introduced when the plastic strain becomes large because in the softening range, the degradation increases rapidly and using the elastic degradation only is not sufficient to represent this phenomenon. A simple model of plastic degradation is:

$$d_p = \kappa^m \tag{2.4.6}$$

where m is a parameter. Note that the value for m is limited, because the degradation of the secant stiffness is coupled with the elastoplastic problem, as discussed in Chapter 3.

Another approach for analyzing inelastic behavior of concrete is to use the continuum damage model in which the stiffness degradation by damage and the plastic deformation are

considered to be coupled [Ju, 1989]. In that model, the concept of the effective stress is used and the plasticity is described not by the stress but by the effective stress. The advantage of that kind of model is that the degradation procedure can be decoupled from the plasticity part by linearizing rate equations. The three-step predictor-corrector method is introduced to solve the system of nonlinear differential equations. The damage evolution (elastic and plastic) is computed after the computation of all internal variables for the plasticity and the effective stress are done. In spite of simplicity of the model, that kind of the continuum damage model has some disadvantages:

1) The plasticity is described on the effective stress, therefore it is difficult to control the parameters which are used in the flow rule and the yield function, because most experimental data are based on the stress.
2) In numerical implementation, the derived elastoplastic tangent is very complicated and expensive to compute. Furthermore, the algorithmic tangent of that model, which is preferred to obtain the quadratic convergent rate, would be more complicated than the elastoplastic one.

Nevertheless, it is noted that decoupling the damage part from the plasticity part in the discretization stage is a good approach for preventing the spurious plastic unloading during iteration or inconsistency of the state in an iterative step.

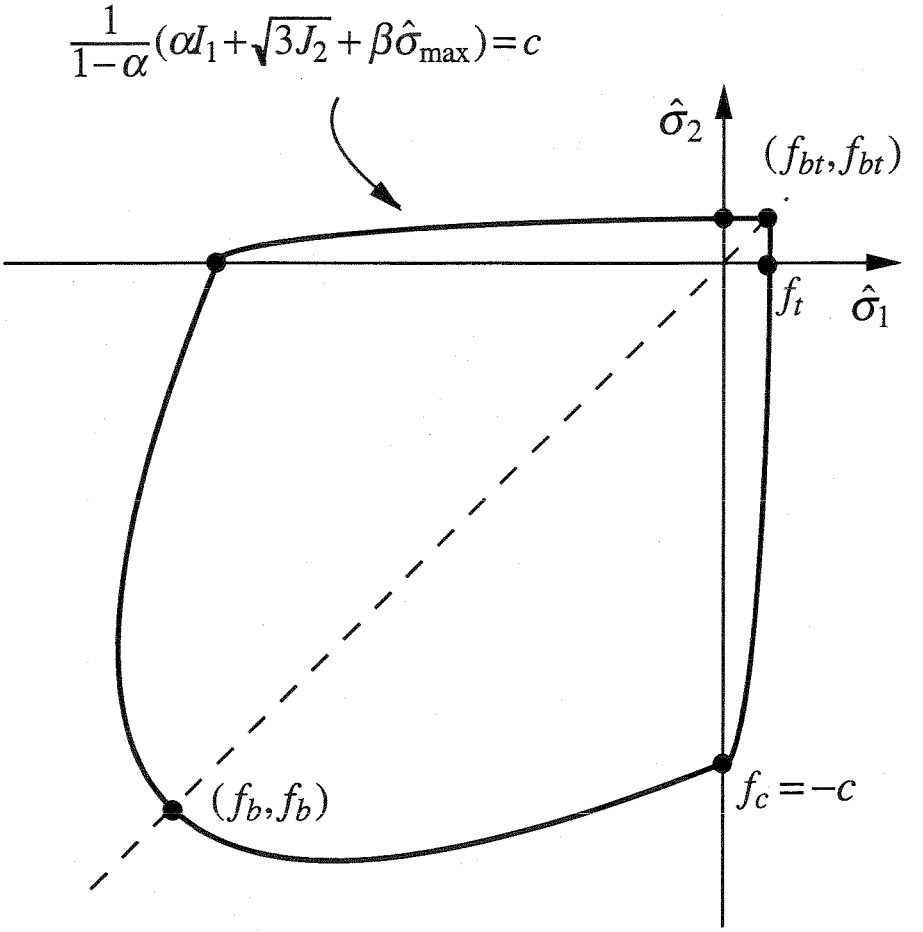

Fig. 2.1 Yield Surface in Two-Dimensional Principal stress plane

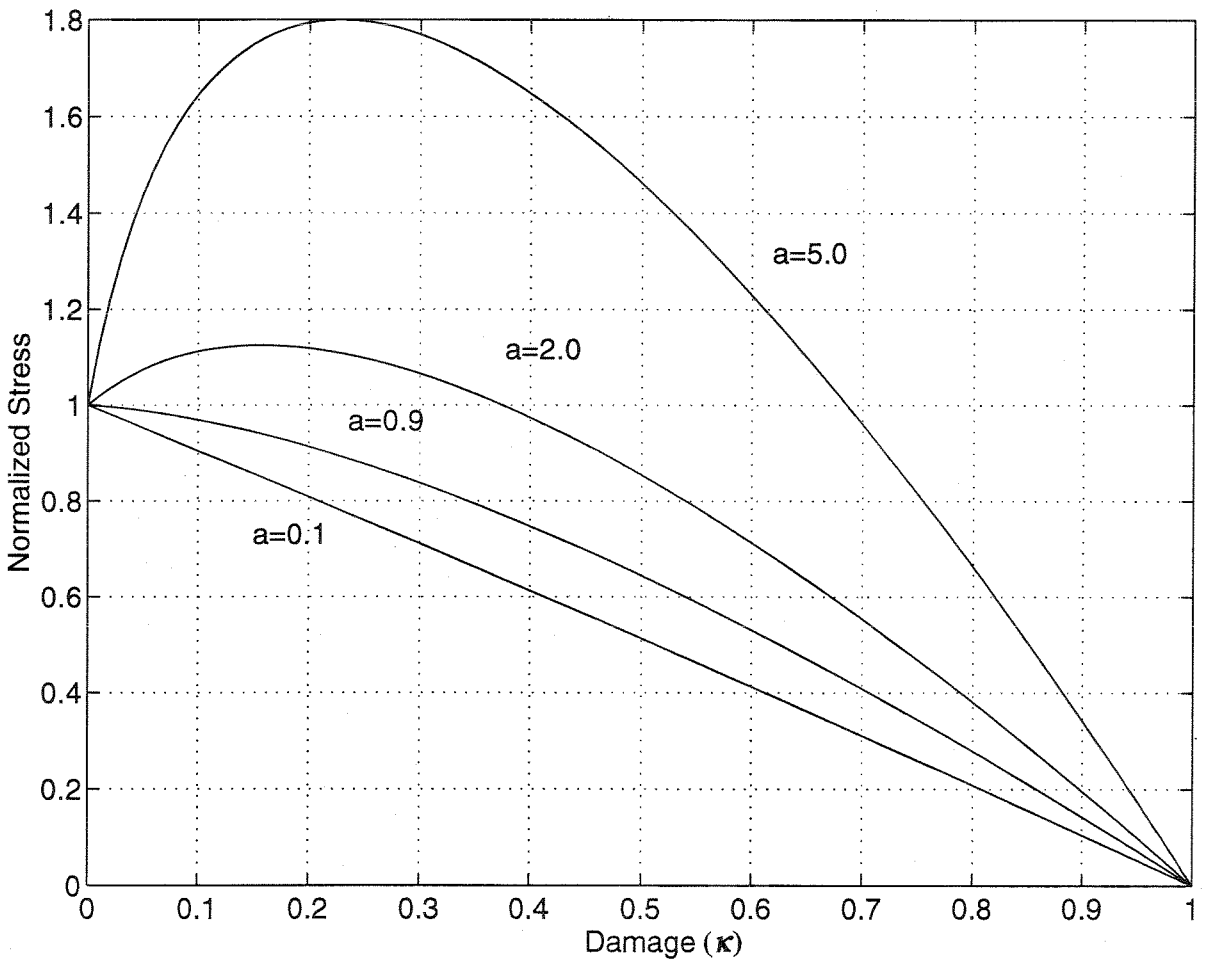

Fig. 2.2 Normalized Stress (f_{ty}=f_{cy}=1) - Damage(κ) Curve

This page is left blank

Chapter 3

NUMERICAL IMPLEMENTATION

3.1 Introduction

In this chapter, the nonlinear differential equations in Chapter 2 are integrated by the backward-Euler method which is known to be unconditionally stable [Ortiz and Popov, 1985]. Because the backward-Euler method is an implicit scheme, an iterative method is required to obtain the converged state. The return-map method has been widely used as the iterative method with the backward-Euler method in computational plasticity.

In this study, a new version of the return-map algorithm is developed because versions of the return-map algorithm, which have been used in various problems, are not appropriate for the model given in Chapter 2. The new return-map algorithm, which is called *the spectral return-map algorithm*, uses a simple tool for problems requiring computation of the principal stresses and the principal plastic strains during iteration.

In this chapter, the general nonlinear solution procedure in the finite element method is summarized first, and the procedures to compute the stresses and the tangent stiffness are given. Note that the matrix-vector notation is used in the following, except Section 3.3.1 in which the use of the tensor notation is still convenient. The following notational convention is also used:

1) $x_n^{(k)}$ represents x at the local iteration step k in the time step n.
2) For simplicity, two often-used differences are defined by:
   $\Delta x = x_{n+1} - x_n$ and $\delta x = x_{n+1}^{(k+1)} - x_{n+1}^{(k)}$

3.2 Nonlinear Solution Procedure

The general numerical procedure to solve nonlinear problems is described in many textbooks (e.g., Crisfield, 1991; Zienkiewicz and Taylor, 1991). The general nonlinear problems can be written in the form:

$$\boldsymbol{\Psi}_{n+1} \equiv \mathbf{P}^{int}(\mathbf{u}_{n+1}) - \mathbf{P}^{ext} = \mathbf{0} \tag{3.2.1}$$

where,

$\mathbf{P}^{int}$: the vector of the internal forces

$\mathbf{P}^{ext}$: the vector of the external forces.

The internal force is evaluated by:

$$\mathbf{P}^{int} = \int_{\Omega} \mathbf{B}^{\mathrm{T}} \boldsymbol{\sigma} d\Omega \tag{3.2.2}$$

The stress at Step $(n+1)$ is given by:

$$\boldsymbol{\sigma}_{n+1} = \boldsymbol{\sigma}_n + f_{\sigma}(\nabla^{(s)} \mathbf{u}_{n+1}, \boldsymbol{\sigma}_{n+1}) \tag{3.2.3}$$

where f_{σ} is a nonlinear function of $\mathbf{u}_{n+1}$ and $\boldsymbol{\sigma}_{n+1}$.

In Eq. 3.2.1, $\mathbf{P}^{ext}$ is a given value and $\mathbf{P}^{int}$ is a nonlinear function of the unknown $\mathbf{u}_{n+1}$. Since f_{σ} is a highly nonlinear function, Eq. 3.2.1 is solved using an iterative method such as the Newton-Raphson (which is called the global iteration in this study). The basic algorithm to solve the nonlinear equation, Eq. 3.2.1, for each increment of the external load force $\Delta\mathbf{P}^{ext}$ is:

1. $\Delta\mathbf{u} = 0$
2. $\mathbf{P}_{n+1}^{ext} = \mathbf{P}_n^{ext} + \Delta\mathbf{P}^{ext}$
3. $\mathbf{u}_{n+1} = \mathbf{u}_n + \Delta\mathbf{u}$
4. $\boldsymbol{\varepsilon}_{n+1} = \nabla^{(s)} \mathbf{u}_{n+1}$
5. Compute $\boldsymbol{\sigma}_{n+1}$
6. $\mathbf{P}^{int} = \int_{\Omega} \mathbf{B}^{\mathrm{T}} \boldsymbol{\sigma} d\Omega$
7. $\Psi_{n+1} = \mathbf{P}^{int} - \mathbf{P}^{ext}$
8. If $\Psi_{n+1} \leq Tolerance$, then solution complete for $\Delta\mathbf{P}^{ext}$
9. Compute new $\Delta\mathbf{u}$ using any iterative method like Newton-Raphson method
10. Go to Step 3

At Step 5, another iteration procedure may be needed to integrate stresses accurately. This procedure (which is called the local iteration in this study) is described in subsequent sections in this chapter.

3.3 Spectral Return-map Algorithm

3.3.1 Return-map Algorithm with Stiffness Degradation

The stress and the plastic strain at Step ($n+1$) can be expressed:

$$\boldsymbol{\sigma}_{n+1} = \boldsymbol{\sigma}_n + \Delta\boldsymbol{\sigma} \tag{3.3.1a}$$

$$\boldsymbol{\varepsilon}^p_{n+1} = \boldsymbol{\varepsilon}^p_n + \Delta\boldsymbol{\varepsilon}^p \tag{3.3.1b}$$

From Eq. 2.2.4, the total stress is written in the form:

$$\begin{aligned}\boldsymbol{\sigma}_{n+1} &= (1-d_{n+1})\mathbf{D}_0 : (\boldsymbol{\varepsilon}_{n+1} - \boldsymbol{\varepsilon}^p_{n+1}) \\ &= \boldsymbol{\sigma}^*_{n+1} - (1-d_{n+1})\mathbf{D}_0 : \Delta\boldsymbol{\varepsilon}^p - \frac{\Delta d}{(1-(d_e)_{n+1})(1-(d_p)_n)}\boldsymbol{\sigma}^*_{n+1} \\ &= \frac{1-(d_p)_{n+1}}{1-(d_p)_n}\boldsymbol{\sigma}^*_{n+1} - (1-d_{n+1})\mathbf{D}_0 : \Delta\boldsymbol{\varepsilon}^p\end{aligned} \tag{3.3.2}$$

where the trial stress is:

$$\boldsymbol{\sigma}^*_{n+1} = (1-(d_e)_{n+1})(1-(d_p)_n)\mathbf{D}_0 : (\boldsymbol{\varepsilon}_{n+1} - \boldsymbol{\varepsilon}^p_n) \tag{3.3.3}$$

Eq. 3.3.2 can be interpreted as the predictor-corrector method which gives:

- Elastic predictor : $\boldsymbol{\sigma}^*_{n+1}$ (3.3.4a)

- Plastic and Damage corrector : $-(1-d_{n+1})\mathbf{D}_0 : \Delta\boldsymbol{\varepsilon}^p - \frac{\Delta d}{(1-(d_e)_{n+1})(1-(d_p)_n)}\boldsymbol{\sigma}^*_{n+1}$ (3.3.4b)

Note that the damage corrector part is not implemented separately, since it is coupled with the plastic corrector part. The backward-Euler method is used to integrate the plastic strain:

$$\begin{aligned}\boldsymbol{\varepsilon}_{n+1}^{p} &= \boldsymbol{\varepsilon}_{n}^{p} + \Delta\boldsymbol{\varepsilon}^{p} \\ &= \sum_{i=1}^{2} \Delta\lambda_i \frac{\partial G_i}{\partial \boldsymbol{\sigma}_{n+1}}\end{aligned} \tag{3.3.5}$$

Eq. 3.3.5 can be rewritten in the split form:

$$\Delta\mathbf{e}_{n+1}^{p} = \Delta\lambda_1 \tilde{\mathbf{g}}_{n+1} \tag{3.3.6a}$$

$$\Delta\theta_{n+1}^{p} = 3\Delta\lambda_2 \mathbf{I} \tag{3.3.6b}$$

where $\mathbf{I}$ is the identity matrix.

In the following, λ_1 and λ_2 are used instead of $\Delta\lambda_1$ and $\Delta\lambda_2$, respectively. In three-dimensional problems, Eq. 3.3.2 can be rewritten by substituting Eq. 3.3.6 and using Eq. 2.2.7:

$$\boldsymbol{\sigma}_{n+1} = \omega\boldsymbol{\sigma}_{n+1}^{*} - (1-d_{n+1})(2G_0\lambda_1\tilde{\mathbf{g}}_{n+1} + 3K_0\lambda_2\mathbf{I}) \tag{3.3.7}$$

where $\omega = \dfrac{1-(d_p)_{n+1}}{1-(d_p)_n}$. Here the stress tensors can be expressed in 3-by-3 matrices. Note that in Eq. 3.3.7, the stress is the second-order symmetric tensor.

From the Kuhn-Tucker conditions discussed in Section 2.2.2, the current state is elastic loading/unloading if the elastic predictor of Eq. 3.3.4a satisfies:

$$\Im(\boldsymbol{\sigma}_{n+1}^{*}, c_n) < 0 \tag{3.3.8}$$

If the current step is evaluated to be in an elastic state, the trial stress is admissible, which means it is accepted as the real stress for the given strain. Accordingly, if Eq. 3.3.8 is satisfied, then:

$$\boldsymbol{\sigma}_{n+1} = \boldsymbol{\sigma}_{n+1}^{*} \tag{3.3.9a}$$

$$\boldsymbol{\varepsilon}^{p}_{n+1} = \boldsymbol{\varepsilon}^{p}_{n} \tag{3.3.9b}$$

$$c_{n+1} = c_n \tag{3.3.9c}$$

$$\kappa_{n+1} = \kappa_n \tag{3.3.9d}$$

With these values, the elastic tangent stiffness, which is assembled for the global iteration, is computed. The formulation of the elastic tangent stiffness is given in Section 3.6. If Eq. 3.3.8 is not satisfied, the stress should be iterated through the plastic corrector algorithm to satisfy the consistency condition such that:

$$F(\boldsymbol{\sigma}_{n+1}) - c(\boldsymbol{\sigma}_{n+1}, \kappa_{n+1}) = 0 \tag{3.3.10}$$

The elastic predictor step gives important information not only about the state of the current step, but also about the eigenvectors of the stress, which plays a crucial role in the next section.

3.3.2 Spectral Decomposition of Return-map

In this section, the second-order tensor, such as stresses and deviatoric plastic strains, is expressed in a 3-by-3 matrix. Let us assume that all c_i are scalar values and the plastic deviatoric strain is the function such that:

$$\tilde{\mathbf{g}} = c_1\boldsymbol{\sigma} + c_2\boldsymbol{\sigma}^{*} + c_3\mathbf{I} \tag{3.3.11}$$

The return-map equation, Eq. 3.3.7, can be simplified to the form:

$$\boldsymbol{\sigma} = \omega\boldsymbol{\sigma}^{*} - \Delta\boldsymbol{\sigma}^{p} \tag{3.3.12}$$

where $\Delta\boldsymbol{\sigma}^{p}$ represents the corrector part in Eq. 3.3.4b. The plastic corrector can be written in the form:

$$\Delta\boldsymbol{\sigma}^{p} = c_4\tilde{\mathbf{g}} + c_5\mathbf{I} \tag{3.3.13}$$

After substituting Eq. 3.3.11 into Eq. 3.3.13, combining Eq. 3.3.12 and Eq. 3.3.13 gives the matrix equation in the form:

$$\boldsymbol{\sigma} = c_6\boldsymbol{\sigma}^{*} + c_7\mathbf{I} \tag{3.3.14}$$

Because $\boldsymbol{\sigma}^{*}$ is a symmetric matrix, it can be factorized by the spectral decomposition:

$$\boldsymbol{\sigma}^{*} = \mathbf{P}\hat{\boldsymbol{\sigma}}^{*}\mathbf{P}^{T} \tag{3.3.15}$$

where $\mathbf{P}$ is the non-singular matrix whose columns are the orthonormal eigenvectors of $\boldsymbol{\sigma}^{*}$ and $\hat{\boldsymbol{\sigma}}^{*}$ is the diagonal matrix of eigenvalues of $\boldsymbol{\sigma}^{*}$. From Eq. 3.3.14 and Eq. 3.3.15, we have:

$$\begin{aligned}\boldsymbol{\sigma} &= \mathbf{P}(c_6\hat{\boldsymbol{\sigma}}^{*})\mathbf{P}^{T} + \mathbf{P}(c_7\mathbf{I})\mathbf{P}^{T} \\ &= \mathbf{P}(c_6\hat{\boldsymbol{\sigma}}^{*} + c_7\mathbf{I})\mathbf{P}^{T}\end{aligned} \tag{3.3.16}$$

Since the spectral decomposition of a symmetric matrix is always available and gives the eigenvectors and eigenvalues of the matrix [Strang, 1980], the stress matrix can be factorized in the form:

$$\boldsymbol{\sigma} = \mathbf{P}\hat{\boldsymbol{\sigma}}\mathbf{P}^{T} \tag{3.3.17}$$

where $\hat{\boldsymbol{\sigma}} = c_6\hat{\boldsymbol{\sigma}}^{*} + c_7\mathbf{I}$ is the diagonal matrix having the principal stresses. Eq. 3.3.17 means that the eigenvectors of the stress are the same as those of the trial stress. Here are two important remarks about the spectral decomposition of the return-map equation.

REMARK 1: The eigenvectors are preserved through the corrector phase. In other words, the eigenvectors of the stress are known in the predictor phase and only the principal stress is needed to be determined in the corrector phase.

REMARK 2: The order of the eigenvalues is preserved through the corrector phase. This is easily verified by observing Eq. 3.3.16. That is, since the stress is computed only by scalar multiplication and constant-vector addition on the trial stress, the order of the diagonal entries in the trial-stress matrix cannot be changed.

By substituting Eq. 3.3.15 and Eq. 3.3.17, the return-map Eq. 3.3.7 is decomposed:

$$\begin{aligned}\boldsymbol{\sigma} &= \mathbf{P}(\omega\hat{\boldsymbol{\sigma}}^*)\mathbf{P}^T - (1-d)\{2G_0\lambda_1\frac{3}{2\sqrt{3J_2}}(\mathbf{P}\hat{\boldsymbol{\sigma}}\mathbf{P}^T - \frac{I_1}{3}\mathbf{P}\mathbf{P}^T) + 3K_0\lambda_2\mathbf{P}\mathbf{P}^T\} \\ &= \mathbf{P}[\omega\hat{\boldsymbol{\sigma}}^* - (1-d)\{2G_0\lambda_1\frac{3}{2\sqrt{3J_2}}(\hat{\boldsymbol{\sigma}} - \frac{I_1}{3}\mathbf{I}) + 3K_0\lambda_2\mathbf{I}\}]\mathbf{P}^T\end{aligned} \tag{3.3.18}$$

Comparing with Eq. 3.3.17, Eq 3.3.18 gives the decoupled return-map equation for the principal stress:

$$\hat{\boldsymbol{\sigma}} = \omega\hat{\boldsymbol{\sigma}}^* - (1-d)\{2G_0\lambda_1\frac{3}{2\sqrt{3J_2}}(\hat{\boldsymbol{\sigma}} - \frac{I_1}{3}\mathbf{I}) + 3K_0\lambda_2\mathbf{I}\} \tag{3.3.19}$$

Also the increment of the plastic strain can be decomposed by the same eigenvectors as those of the trial stress:

$$\begin{aligned}\Delta\boldsymbol{\varepsilon}^p &= \lambda_1\frac{3}{2\sqrt{3J_2}}(\mathbf{P}\hat{\boldsymbol{\sigma}}\mathbf{P}^T - \frac{I_1}{3}\mathbf{P}\mathbf{P}^T) + \lambda_2\mathbf{P}\mathbf{P}^T \\ &= \mathbf{P}[\lambda_1\frac{3}{2\sqrt{3J_2}}(\hat{\boldsymbol{\sigma}} - \frac{I_1}{3}\mathbf{I}) + \lambda_2\mathbf{I}]\mathbf{P}^T\end{aligned} \tag{3.3.20}$$

Accordingly, the eigenvalues of the plastic strain increment are the diagonal entries of the decoupled matrix $\Delta\hat{\boldsymbol{\varepsilon}}^p$:

$$\Delta\hat{\boldsymbol{\varepsilon}}^p = \lambda_1 \frac{3}{2\sqrt{3J_2}}(\hat{\boldsymbol{\sigma}} - \frac{I_1}{3}\mathbf{I}) + \lambda_2 \mathbf{I} \tag{3.3.21}$$

Note that both Eq. 3.3.20 and Eq. 3.3.21 are valid for both three-dimensional and two-dimensional problems.

3.4 Linearization of Damage Evolution Equations

The damage variable κ is evaluated by the evolution law, Eq. 2.3.1, which is the nonlinear function of κ, λ_2 and $\hat{\boldsymbol{\sigma}}$. Through this section, the principal stress, $\hat{\boldsymbol{\sigma}}$, is assumed as the vector which has two components for the plane stress problem and three components for the three-dimensional and plane strain problems. Linearization of the rate equation, Eq. 2.3.1, with the backward-Euler method gives:

$$\kappa_{n+1} = \kappa_n + A(\hat{\boldsymbol{\sigma}}_{n+1}, \kappa_{n+1})\Delta\hat{\varepsilon}_1^p + B(\hat{\boldsymbol{\sigma}}_{n+1}, \kappa_{n+1})\Delta\hat{\varepsilon}_3^p \tag{3.4.1}$$

in which the principal values of the plastic strain are assumed to be ordered in magnitude. In fact, Eq. 3.4.1 is the formulation which requires another iteration in the stress computation procedure. The Newton-Raphson method is used to solve Eq. 3.4.1, which requires one scalar residual equation.

The residual is directly defined from Eq. 3.4.1:

$$Q(\kappa, \lambda_2, \hat{\boldsymbol{\sigma}}) = -\kappa_{n+1} + \kappa_n + A(\hat{\boldsymbol{\sigma}}_{n+1}, \kappa_{n+1})\Delta\hat{\varepsilon}_1^p + B(\hat{\boldsymbol{\sigma}}_{n+1}, \kappa_{n+1})\Delta\hat{\varepsilon}_3^p \tag{3.4.2}$$

The total differential of residual Q becomes:

$$dQ = \frac{\partial Q}{\partial \kappa} d\kappa + \frac{\partial Q}{\partial \lambda_2} d\lambda_2 + \frac{\partial Q}{\partial \hat{\boldsymbol{\sigma}}} d\hat{\boldsymbol{\sigma}} \tag{3.4.3}$$

and the partial derivatives in Eq. 3.4.3 are given by:

$$\frac{\partial Q}{\partial \kappa} = -1 + \frac{\partial A}{\partial \kappa}\Delta\hat{\varepsilon}_1^p + \frac{\partial B}{\partial \kappa}\Delta\hat{\varepsilon}_3^p + (A\tilde{g}_1 + B\tilde{g}_3)\frac{\partial \lambda_1}{\partial \hat{\boldsymbol{\sigma}}} \tag{3.4.4a}$$

$$\frac{\partial Q}{\partial \lambda_2} = A(\frac{\partial \lambda_1}{\partial \lambda_2}\tilde{g}_1 + 1) + B(\frac{\partial \lambda_1}{\partial \lambda_2}\tilde{g}_3 + 1) \tag{3.4.4b}$$

$$\frac{\partial Q}{\partial \hat{\boldsymbol{\sigma}}} = \frac{\partial A}{\partial \hat{\boldsymbol{\sigma}}}\Delta\hat{\varepsilon}_1^p + \frac{\partial B}{\partial \hat{\boldsymbol{\sigma}}}\Delta\hat{\varepsilon}_3^p + (A\frac{\partial \tilde{g}_1}{\partial \hat{\boldsymbol{\sigma}}} + B\frac{\partial \tilde{g}_3}{\partial \hat{\boldsymbol{\sigma}}})\lambda_1 + (A\tilde{g}_1 + B\tilde{g}_3)\frac{\partial \lambda_1}{\partial \hat{\boldsymbol{\sigma}}} \tag{3.4.4c}$$

The partial derivative of the degradation variable d with respect to κ depends on the definition of degradation models and from the suggested model in Section 2.4, it is given as:

$$\frac{\partial d}{\partial \kappa} = (1 - d_e)\frac{\partial d_p}{\partial \kappa} = (1 - d_e)m\kappa^{m-1} \tag{3.4.5}$$

The rate equation of the cohesion c defined in Section 2.3 is also linearized by using the backward-Euler scheme:

$$c_{n+1} = c_n + r(\hat{\boldsymbol{\sigma}}_{n+1})\Delta c_t(\kappa_{n+1}) + (1 - r(\hat{\boldsymbol{\sigma}}_{n+1}))\Delta c_c(\kappa_{n+1}) \tag{3.4.6}$$

The derivatives of the discretized cohesion c_{n+1} is derived directly from Eq. 3.4.6 in the form as:

$$(\frac{\partial c}{\partial \kappa})_{n+1} = r(\hat{\boldsymbol{\sigma}}_{n+1})(\frac{\partial c_t}{\partial \hat{\boldsymbol{\sigma}}})_{n+1} + (1 - r(\hat{\boldsymbol{\sigma}}_{n+1}))(\frac{\partial c_c}{\partial \hat{\boldsymbol{\sigma}}})_{n+1} \tag{3.4.7a}$$

$$(\frac{\partial c}{\partial \hat{\boldsymbol{\sigma}}})_{n+1} = (\frac{\partial r}{\partial \hat{\boldsymbol{\sigma}}})_{n+1}(\Delta c_t(\kappa_{n+1}) - \Delta c_c(\kappa_{n+1})) \tag{3.4.7b}$$

Applying the chain rule to the consistency condition yields:

$$\frac{\partial F}{\partial \hat{\boldsymbol{\sigma}}} d\hat{\boldsymbol{\sigma}} = (\frac{\partial c}{\partial \hat{\boldsymbol{\sigma}}} \Delta\kappa) d\hat{\boldsymbol{\sigma}} + (\frac{\partial c}{\partial \kappa} \Delta\kappa + c) d\kappa. \tag{3.4.8}$$

Accordingly, the relation between $d\kappa$ and $d\hat{\boldsymbol{\sigma}}$ is obtained from Eq. 3.4.8:

$$d\kappa = \mathbf{T}_{\kappa\sigma} d\hat{\boldsymbol{\sigma}} \tag{3.4.9}$$

where $\mathbf{T}_{\kappa\sigma} = (\frac{\partial F}{\partial \hat{\boldsymbol{\sigma}}} - \frac{\partial c}{\partial \hat{\boldsymbol{\sigma}}} \Delta\kappa) / (\frac{\partial c}{\partial \kappa} \Delta\kappa + c)$. The total differential of the principle stress becomes:

$$d\hat{\boldsymbol{\sigma}} = \frac{\partial \hat{\boldsymbol{\sigma}}}{\partial \lambda_2} d\lambda_2 + \frac{\partial \hat{\boldsymbol{\sigma}}}{\partial \kappa} d\kappa \tag{3.4.10}$$

Substituting Eq. 3.4.10 into Eq. 3.4.9 gives the relation between $d\lambda_2$ and $d\kappa$:

$$d\lambda_2 = S_{\lambda\kappa} d\kappa \tag{3.4.11}$$

where $S_{\lambda\kappa} = \dfrac{1 - \mathbf{T}_{\kappa\sigma}(\dfrac{\partial \hat{\boldsymbol{\sigma}}}{\partial \kappa})}{\mathbf{T}_{\kappa\sigma}(\dfrac{\partial \hat{\boldsymbol{\sigma}}}{\partial \lambda_2})}$

Consequently, we have the scalar Jacobian of Q with respect to κ :

$$\frac{dQ}{d\kappa} = \frac{\partial Q}{\partial \kappa} + \frac{\partial Q}{\partial \hat{\boldsymbol{\sigma}}} \frac{\partial \hat{\boldsymbol{\sigma}}}{\partial \kappa} + (\frac{\partial Q}{\partial \lambda_2} + \frac{\partial Q}{\partial \hat{\boldsymbol{\sigma}}} \frac{\partial \hat{\boldsymbol{\sigma}}}{\partial \lambda_2}) S_{\lambda\kappa} \tag{3.4.12}$$

The $\delta\kappa$ at the $(i+1)$-th iteration is determined by solving the scalar equation:

$$(\frac{dQ}{d\kappa})^{(i)} \delta\kappa = -Q^{(i)} \tag{3.4.13}$$

The result of Eq. 3.4.13 is added to update the damage variable:

$$\kappa_{n+1}^{(i+1)} = \kappa_{n+1}^{(i)} + \delta\kappa \tag{3.4.14}$$

3.5 Plane Stress Formulation

3.5.1 Spectral Return-map Algorithm for Plane Stress

As in Section 3.3.2, a matrix form is used for representing the second-order tensor. In the plane stress problems, the stress-strain relation is given by Eq. 2.2.8. By the process explained in Section 3.3.1, the return-map equation for the plane stress problem becomes:

$$\boldsymbol{\sigma} = \omega\boldsymbol{\sigma}^* - (1-d)\{2G_0\Delta\boldsymbol{\varepsilon}^p + \frac{\nu E_0}{1-\nu^2}(\Delta\varepsilon_{11}^p + \Delta\varepsilon_{22}^p)\mathbf{I}\} \tag{3.5.1}$$

where the stress and, consequently, the trial stress are 2-by-2 matrices corresponding the plane stress. Using the flow rule defined in Section 2.2.3, Eq. 3.5.1 becomes:

$$\boldsymbol{\sigma} = \omega\boldsymbol{\sigma}^* - (1-d)\{2G_0\lambda_1\frac{3}{2\sqrt{3J_2}}(\boldsymbol{\sigma} - \tilde{\nu}\frac{I_1}{3}\mathbf{I}) + 3\tilde{K}_0\lambda_2\mathbf{I}\} \tag{3.5.2}$$

where,

$$\tilde{\nu} = (1-2\nu)/(1-\nu)$$
$$\tilde{K}_0 = E_0/3(1-\nu)$$

Because Eq. 3.5.2 is a special form of Eq. 3.3.12, it can be decoupled by the spectral decomposition explained in Section 3.3.2. Accordingly,

$$\hat{\boldsymbol{\sigma}} = \omega\hat{\boldsymbol{\sigma}}^* - (1-d)\{2G_0\lambda_1\frac{3}{2\sqrt{3J_2}}(\hat{\boldsymbol{\sigma}} - \tilde{\nu}\frac{I_1}{3}\mathbf{I}) + 3\tilde{K}_0\lambda_2\mathbf{I}\} \tag{3.5.3}$$

Eq. 3.5.3 can be simplified by moving $\hat{\boldsymbol{\sigma}}$ from the RHS to the LHS:

$$\hat{\boldsymbol{\sigma}} = \omega\xi\hat{\boldsymbol{\sigma}}^* + \{\tilde{\nu}\frac{I_1}{3}(1-\xi) - 3(1-d)\tilde{K}_0\xi\lambda_2\}\mathbf{I} \tag{3.5.4}$$

where

$$\xi = \sqrt{3J_2}\,/(\sqrt{3J_2} + 3G\lambda_1) \tag{3.5.5}$$

After substituting $I_1 = \hat{\sigma}_1 + \hat{\sigma}_2$ into Eq. 3.5.5, the final form of the return-map equation for the plane stress problem is obtained:

$$\hat{\boldsymbol{\sigma}} = \omega\xi\hat{\boldsymbol{\sigma}}^* + \frac{\xi}{3-2\tilde{\nu}(1-\xi)}\{\tilde{\nu}(1-\xi)\omega I_1^* - 9(1-d)\tilde{K}_0\lambda_2\}\mathbf{I} \tag{3.5.6}$$

where $I_1^* = \hat{\sigma}_1^* + \hat{\sigma}_2^*$.

From Eq. 3.5.6, it is observed that the principal stress is the explicit function of the scalar unknowns:

$$\hat{\boldsymbol{\sigma}} = \overline{\boldsymbol{\sigma}}(\kappa, \xi, \lambda_2) \tag{3.5.7}$$

Eq. 3.5.5 can be written in another functional form:

$$\xi = \xi(\kappa, \lambda_2, \hat{\boldsymbol{\sigma}}) \tag{3.5.8}$$

ξ is eliminated in Eq. 3.5.7 by substituting Eq. 3.5.8. Finally, the principal stress is expressed as:

$$\hat{\boldsymbol{\sigma}} = \hat{\boldsymbol{\sigma}}(\kappa, \lambda_2) \tag{3.5.9}$$

In the rest of Section 3.5, two-dimensional vectors are used instead of the diagonal matrices, such as $\hat{\boldsymbol{\sigma}}$ and $\Delta\hat{\boldsymbol{\varepsilon}}^p$.

3.5.2 $\lambda_1 - \lambda_2$ Relations

The $\lambda_1 - \lambda_2$ relation is very important because the amount of plastic volume change depends on it. Additionally, in terms of algorithm, the $\lambda_1 - \lambda_2$ relation is connected with the existence of the numerical solution.

In the plane stress problem, the region outside of the yield surface is divided into two subregions by a boundary which is defined as:

$$\hat{\boldsymbol{\sigma}}_b^* = \hat{\boldsymbol{\sigma}}_c + s\{\frac{3G_0}{c}(\hat{\boldsymbol{\sigma}}_c + \tilde{v}\frac{c}{3}\mathbf{I}) + 3\tilde{K}_0\alpha_{p1}\mathbf{I}\} \tag{3.5.10}$$

where s is an arbitrary non-negative parameter, α_{p1} is a parameter of the plastic potential in Region 1 and $\hat{\boldsymbol{\sigma}}_c = (0,-c)$. Eq. 3.5.10 is the equation of the line going out from $(0,-c)$ with the angle ϕ in the principal stress plane:

$$\phi = \tan^{-1}(1 - \frac{3(1-\nu)}{2(1+\nu)(\alpha_{p1}-1)+3}) \tag{3.5.11}$$

Note that the angle defined in Eq. 3.5.11 is evaluated only by material properties. Fig. 3.1 shows the relation between ϕ and α_{p1}.

The $\lambda_1 - \lambda_2$ relation should be defined to satisfy the following conditions:

1) Any trial stress can be returned to an unique point on the yield surface in the principal stress plane.
2) The resulted plastic strain should agree with experimental observation.

In this study, λ_2 is assumed to be the function of the principal stress and λ_1:

$$\lambda_2 = \lambda_2(\hat{\boldsymbol{\sigma}}, \kappa, \lambda_1) \tag{3.5.12}$$

In Region 1, the $\lambda_1 - \lambda_2$ relation gives the same plastic strain as if it came from one Drucker-Prager-type plastic potential function with α_{p1}:

$$\lambda_2 = \alpha_{p1}\lambda_1 \tag{3.5.13}$$

λ_2 in Region 2 is defined in different way to satisfy the first condition for the $\lambda_1 - \lambda_2$ relation. The form multiplied by (1+p) in Eq. 3.5.13 is used:

$$\lambda_2 = \alpha_{p2}(1+p)\lambda_1 \tag{3.5.14}$$

p is determined for λ_2 to be continuous at (0,-c) and be changed continuously from that point to the maximum biaxial stress point (σ_b, σ_b), where $\sigma_b = (\frac{1-\alpha}{2\alpha-1})c$. Note that at the maximum biaxial stress point, $\lambda_2 = \alpha_{p2}\lambda_1$, where α_{p2} is a parameter of the plastic potential at that point. If we use linear variation of p with respect to $\hat{\sigma}_1$,

$$p = p(\hat{\boldsymbol{\sigma}}, \kappa) = (\frac{\alpha_{p1} - \alpha_{p2}}{\alpha_{p2}})(1 - \frac{\hat{\sigma}_1}{\sigma_b(\hat{\boldsymbol{\sigma}}, \kappa)}) \tag{3.5.15}$$

Because Eq. 3.5.13 can be understood as the special case of Eq. 3.5.14, we need only one general form for $\lambda_1 - \lambda_2$ relation such that:

$$\lambda_2 = \alpha_p(1+p)\lambda_1 \tag{3.5.16}$$

where in Region 1, p=0 and $\alpha_p = \alpha_{p1}$ and in Region 2, p is given as Eq. 3.5.15 and $\alpha_p = \alpha_{p2}$. The geometric interpretation is illustrated in Fig. 3.2.

The total differential of Eq. 3.5.16 becomes:

$$d\lambda_1 = \frac{\partial \lambda_1}{\partial \lambda_2} d\lambda_2 + \frac{\partial \lambda_1}{\partial \hat{\boldsymbol{\sigma}}} d\hat{\boldsymbol{\sigma}} + \frac{\partial \lambda_1}{\partial \kappa} d\kappa \tag{3.5.17}$$

where,

$$\frac{\partial \lambda_1}{\partial \lambda_2} = \frac{1}{\alpha_p (1+p)} \tag{3.5.18a}$$

$$\frac{\partial \lambda_1}{\partial \hat{\boldsymbol{\sigma}}} = \frac{\lambda_1}{(1+p)} \frac{\partial p}{\partial \hat{\boldsymbol{\sigma}}} \tag{3.5.18b}$$

$$\frac{\partial \lambda_1}{\partial \kappa} = \frac{-\lambda_1}{(1+p)} \frac{\partial p}{\partial \kappa} \tag{3.5.18c}$$

3.5.3 Computation of Stress

For the given damage variable, κ, the stress is computed to satisfy the consistency condition by the iterative scheme such as the Newton-Raphson method. Since two principal stresses are unknown, two residual equations are required to define the nonlinear problem. One residual comes from the consistency condition and the other residual is derived from Eq. 3.5.5:

$$\Im(\hat{\boldsymbol{\sigma}}) = F(\hat{\boldsymbol{\sigma}}) - c(\hat{\boldsymbol{\sigma}}) \tag{3.5.19a}$$

$$X(\hat{\boldsymbol{\sigma}}, \xi, \lambda_2) = \xi\{\alpha_{p2}(1+p)\sqrt{3J_2} + 3G\lambda_2\} - \alpha_{p2}(1+p)\sqrt{3J_2} \tag{3.5.19b}$$

In fact, it is more convenient to use ξ and λ_2 as independent unknowns rather than the principal stress itself. By Eq. 3.5.7 and the chain rule, the total differentials of 3.5.19 become:

$$d\Im = \left(\frac{\partial F}{\partial \hat{\boldsymbol{\sigma}}} - \frac{\partial c}{\partial \hat{\boldsymbol{\sigma}}}\right) \frac{\partial \overline{\boldsymbol{\sigma}}}{\partial \xi} d\xi + \left(\frac{\partial F}{\partial \hat{\boldsymbol{\sigma}}} - \frac{\partial c}{\partial \hat{\boldsymbol{\sigma}}}\right) \frac{\partial \overline{\boldsymbol{\sigma}}}{\partial \lambda_2} d\lambda_2 \tag{3.5.20a}$$

$$dX = \left(\frac{\partial X}{\partial \hat{\boldsymbol{\sigma}}} \frac{\partial \overline{\boldsymbol{\sigma}}}{\partial \xi} + \frac{\partial X}{\partial \xi}\right) d\xi + \left(\frac{\partial X}{\partial \hat{\boldsymbol{\sigma}}} \frac{\partial \overline{\boldsymbol{\sigma}}}{\partial \lambda_2} + \frac{\partial X}{\partial \lambda_2}\right) d\lambda_2 \tag{3.5.20b}$$

The Newton-Raphson formulation of the nonlinear system is derived by linearizing Eq. 3.5.20 and setting the next residuals to be zero. Let us define the linear increments of $d\xi$ and $d\lambda_2$ are $\delta\xi$ and $\delta\lambda_2$, respectively. The Newton-Raphson algorithm in matrix form is given by:

$$\begin{bmatrix} \dfrac{\partial \mathfrak{I}}{\partial \hat{\boldsymbol{\sigma}}}\dfrac{\partial \overline{\boldsymbol{\sigma}}}{\partial \xi} & \dfrac{\partial \mathfrak{I}}{\partial \hat{\boldsymbol{\sigma}}}\dfrac{\partial \overline{\boldsymbol{\sigma}}}{\partial \lambda_2} \\ \dfrac{\partial X}{\partial \hat{\boldsymbol{\sigma}}}\dfrac{\partial \overline{\boldsymbol{\sigma}}}{\partial \xi}+\dfrac{\partial X}{\partial \xi} & \dfrac{\partial X}{\partial \hat{\boldsymbol{\sigma}}}\dfrac{\partial \overline{\boldsymbol{\sigma}}}{\partial \lambda_2}+\dfrac{\partial X}{\partial \lambda_2} \end{bmatrix} \begin{bmatrix} \delta\xi \\ \delta\lambda_2 \end{bmatrix} = \begin{bmatrix} -\mathfrak{I} \\ -X \end{bmatrix} \tag{3.5.21}$$

where (k) means the results from the (k)-th iteration. After solving Eq. 3.5.21, both unknowns are updated:

$$\xi^{(k+1)} = \xi^{(k)} + \delta\xi \tag{3.5.22a}$$

$$\lambda_2^{(k+1)} = \lambda_2^{(k)} + \delta\lambda_2 \tag{3.5.22b}$$

The principal stress at the $(k+1)$-th step is computed by Eq. 3.5.6. The iteration is continued until a norm of the residuals becomes smaller than a certain tolerance. If we use the 2-norm of the residuals as the tolerance, the stop-condition of the iteration becomes:

$$\frac{1}{c_0}\sqrt{X^2 + \mathfrak{I}^2} \le Tolerance \tag{3.5.23}$$

3.6 Algorithmic Tangent Stiffness

If Newton-Raphson-type methods are used in the global iteration algorithm, which is described in Section 3.1, the rate of convergence is strongly dependent on the elastoplastic tangent stiffness. It has been known that the quadratic convergence cannot be obtained, unless the algorithmic tangent stiffness matrix, which is consistent with the local iteration algorithm, is used in the global iteration [Simo and Taylor, 1985 and 1986]. The

algorithmic tangent stiffness is defined by combining the linearized equations that have been used in the local iteration algorithm. Therefore, the form of the algorithmic tangent stiffness depends on the algorithm used to compute stresses.

After getting the converged stresses and internal variables for the given strain, all the residual equations are assumed to be satisfied:

$$\mathbf{D}_0^{-1}\boldsymbol{\sigma} = (1-d_e)(1-d_p)(\boldsymbol{\varepsilon}-\boldsymbol{\varepsilon}^p) \tag{3.6.1a}$$

$$Q(\hat{\boldsymbol{\sigma}}, \lambda_2, \kappa) = 0 \tag{3.6.1b}$$

$$\Im(\hat{\boldsymbol{\sigma}}, \kappa) = 0 \tag{3.6.1c}$$

The total differential of Eq. 3.6.1a becomes:

$$\mathbf{D}_0^{-1} d\boldsymbol{\sigma} = -\{(1-d_e)\frac{\partial d_p}{\partial \kappa} d\kappa + (1-d_p)\frac{\partial d_e}{\partial \boldsymbol{\varepsilon}} d\boldsymbol{\varepsilon}\}(\boldsymbol{\varepsilon}-\boldsymbol{\varepsilon}^p) + (1-d)(d\boldsymbol{\varepsilon} - d\boldsymbol{\varepsilon}^p) \tag{3.6.2}$$

in which the total differential of the plastic strain is:

$$d\boldsymbol{\varepsilon}^p = \tilde{\mathbf{g}} d\lambda_1 + \lambda_1 d\tilde{\mathbf{g}} + d\lambda_2 \mathbf{I} \tag{3.6.3}$$

and,

$$\frac{\partial d_e}{\partial \boldsymbol{\varepsilon}} = \frac{\partial d_e}{\partial \hat{\varepsilon}_{\max}} \frac{\partial \hat{\varepsilon}_{\max}}{\partial \boldsymbol{\varepsilon}} \tag{3.6.4}$$

From Eq. 3.6.1b, the total differential of Q becomes zero:

$$\frac{\partial Q}{\partial \hat{\boldsymbol{\sigma}}} d\hat{\boldsymbol{\sigma}} + \frac{\partial Q}{\partial \lambda_2} d\lambda_2 + \frac{\partial Q}{\partial \kappa} d\kappa = 0 \tag{3.6.5}$$

Combining Eq. 3.4.9 and Eq. 3.6.5 gives:

$$d\lambda_2 = \mathbf{T}_{\lambda\sigma} d\hat{\boldsymbol{\sigma}} \tag{3.6.6}$$

where,

$$\mathbf{T}_{\lambda\sigma} = \frac{\dfrac{\partial Q}{\partial \hat{\boldsymbol{\sigma}}} + \dfrac{\partial Q}{\partial \kappa}\mathbf{T}_{\kappa\sigma}}{-\dfrac{\partial Q}{\partial \lambda_2}} \tag{3.6.7}$$

Substituting Eq. 3.6.6 into Eq. 3.6.3 yields:

$$d\boldsymbol{\varepsilon}^p = (\mathbf{V}_{\varepsilon\lambda}\mathbf{T}_{\lambda\sigma} + \mathbf{M}_{\sigma\varepsilon}) d\hat{\boldsymbol{\sigma}} + \lambda_1 \frac{\partial \tilde{\mathbf{g}}}{\partial \boldsymbol{\sigma}} d\boldsymbol{\sigma} \tag{3.6.8}$$

where,

$$\mathbf{V}_{\varepsilon\lambda} = \left(\frac{\partial \lambda_1}{\partial \lambda_2}\tilde{\mathbf{g}} + \mathbf{I}\right) \tag{3.6.9}$$

$$\mathbf{M}_{\sigma\varepsilon} = \tilde{\mathbf{g}} \frac{\partial \lambda_1}{\partial \hat{\boldsymbol{\sigma}}} \tag{3.6.10}$$

The total differentials of the stress and the principal stress are related by the chain rule:

$$d\hat{\boldsymbol{\sigma}} = \frac{\partial \hat{\boldsymbol{\sigma}}}{\partial \boldsymbol{\sigma}} d\boldsymbol{\sigma} \tag{3.6.11}$$

Finally, substituting Eq. 3.6.8 combined with Eq. 3.6.11 into Eq. 3.6.2 yields:

$$[\mathbf{D}_0^{-1} + \{(1-d_e)\frac{\partial d}{\partial \kappa}(\boldsymbol{\varepsilon}-\boldsymbol{\varepsilon}^p)\mathbf{T}_{\kappa\sigma} + (1-d)(\mathbf{V}_{\varepsilon\lambda}\mathbf{T}_{\lambda\sigma} + \mathbf{M}_{\sigma\varepsilon})\}\frac{\partial \hat{\boldsymbol{\sigma}}}{\partial \boldsymbol{\sigma}} + (1-d)\lambda_1 \frac{\partial \tilde{\mathbf{g}}}{\partial \boldsymbol{\sigma}}]d\boldsymbol{\sigma}$$
$$= \{(1-d)\mathbf{I} - (1-d_p)(\boldsymbol{\varepsilon}-\boldsymbol{\varepsilon}^p)\frac{\partial d_e}{\partial \boldsymbol{\varepsilon}}\}d\boldsymbol{\varepsilon} \tag{3.6.12}$$

After imposing the inverse operation on Eq. 3.6.12, the algorithmic tangent stiffness can be written in the form:

$$\left.\frac{d\boldsymbol{\sigma}}{d\boldsymbol{\varepsilon}}\right|_{n+1} = [\mathbf{D}^{-1} + \{\frac{1}{(1-d_p)}\frac{\partial d_p}{\partial \kappa}(\boldsymbol{\varepsilon}-\boldsymbol{\varepsilon}^p)\mathbf{T}_{\kappa\sigma} + \mathbf{V}_{\varepsilon\lambda}\mathbf{T}_{\lambda\sigma} + \mathbf{M}_{\sigma\varepsilon}\}\frac{\partial \hat{\boldsymbol{\sigma}}}{\partial \boldsymbol{\sigma}} + \lambda_1 \frac{\partial \tilde{\mathbf{g}}}{\partial \boldsymbol{\sigma}}]^{-1}$$
$$\{\mathbf{I} - \frac{1}{(1-d_e)}(\boldsymbol{\varepsilon}-\boldsymbol{\varepsilon}^p)\frac{\partial d_e}{\partial \boldsymbol{\varepsilon}}\} \tag{3.6.13}$$

The elastic tangent stiffness is computed if the given strain results in the elastic unloading state. From Eq. 3.3.2, the total differentials are:

$$d\boldsymbol{\sigma} = \frac{-d(d_e)}{(1-d_e)}\boldsymbol{\sigma}^* + (1-d_p)(1-d_e)\mathbf{D}_0 d\boldsymbol{\varepsilon} \tag{3.6.14}$$

From Eq. 2.4.5, the total differential of the elastic degradation variable becomes:

$$d(d_e) = \frac{\partial d_e}{\partial \boldsymbol{\varepsilon}}d\boldsymbol{\varepsilon} \tag{3.6.15}$$

Substituting Eq. 3.6.15 into Eq. 3.6.14 gives the elastic tangent stiffness matrix:

$$\left.\frac{d\boldsymbol{\sigma}}{d\boldsymbol{\varepsilon}}\right|_{n+1} = (1-d)\mathbf{D}_0 - \frac{1}{(1-d_e)}\boldsymbol{\sigma}^*\frac{\partial d_e}{\partial \boldsymbol{\varepsilon}} \tag{3.6.16}$$

3.7 Summary of Algorithm

The spectral return-map algorithm is summarized in this section, for the plane stress formulation. The algorithm is embedded, as the local iteration procedure, in Step 5 of the global iteration algorithm, which is described in Section 3.2. The initial condition consists of the given values:

$$\boldsymbol{\varepsilon}_{n+1},\ \boldsymbol{\varepsilon}_n^p,\ \kappa_n,\ c_n$$

1. Determine the elastic degradation $(d_e)_{n+1}$ by Eq. 2.4.3
2. Compute the trial stress:

$$\boldsymbol{\sigma}_{n+1}^* = (1-(d_e)_{n+1})(1-(d_p)_n)\mathbf{D}_0(\boldsymbol{\varepsilon}_{n+1}-\boldsymbol{\varepsilon}_n^p)$$

3. If $\Im(\sigma_{n+1}^*, c_n) < 0$ (Elastic state):

   3.1 $\boldsymbol{\sigma}_{n+1} = \boldsymbol{\sigma}_{n+1}^*$, $\boldsymbol{\varepsilon}_{n+1}^p = \boldsymbol{\varepsilon}_n^P$, $c_{n+1} = c_n$, $\kappa_{n+1} = \kappa_n$

   3.2 Compute the elastic tangent stiffness matrix:

$$\left.\frac{d\boldsymbol{\sigma}}{d\boldsymbol{\varepsilon}}\right|_{n+1} = (1-d)\mathbf{D}_0 - \frac{1}{(1-d_e)}\boldsymbol{\sigma}^*\frac{\partial d_e}{\partial \boldsymbol{\varepsilon}}$$

4. Else (Plastic state):

   4.1 Decompose the trial stress:

$$\boldsymbol{\sigma}_{n+1}^* = \mathbf{P}\hat{\boldsymbol{\sigma}}_{n+1}^*\mathbf{P}^T$$

   4.2 Set the initial values:

$$\boldsymbol{\sigma} = \boldsymbol{\sigma}_{n+1}^*;\ \boldsymbol{\varepsilon}^p = \boldsymbol{\varepsilon}_n^P;\ c = c_n;\ \kappa = \kappa_n$$

   4.3 Compute the residual:

$$Q = -\kappa + \kappa_n + A(\hat{\boldsymbol{\sigma}},\kappa)\Delta\hat{\varepsilon}_1^p + B(\hat{\boldsymbol{\sigma}},\kappa)\Delta\hat{\varepsilon}_3^p$$

   4.4 If $Q \le$ *Tolerance*, then go to Step 4.10

   4.5 Solve $(\frac{dQ}{d\kappa})\delta\kappa = -Q$

   4.6 Update the damage variable and the plastic degradation:

$$\kappa = \kappa + \delta\kappa$$

$$d_p = \kappa^m$$

   4.7 For the given κ, compute $\hat{\boldsymbol{\sigma}}$ and c by the Newton-Raphson scheme:

   4.7.1 Determine the region by Eq. 3.5.11

4.7.2 Compute p

4.7.3 Compute the residuals:

$$\Im(\hat{\boldsymbol{\sigma}}) = F(\hat{\boldsymbol{\sigma}}) - c(\hat{\boldsymbol{\sigma}})$$

$$X(\hat{\boldsymbol{\sigma}}, \xi, \lambda_2) = \xi\{\alpha_{p2}(1+p)\sqrt{3J_2} + 3G\lambda_2\} - \alpha_{p2}(1+p)\sqrt{3J_2}$$

4.7.4 If $\frac{1}{c_0}\sqrt{X^2 + \Im^2} \le Tolerance$, then go to Step 4.3

4.7.5 Solve the linearized equation:

$$\begin{bmatrix} \frac{\partial \Im}{\partial \hat{\boldsymbol{\sigma}}}\frac{\partial \overline{\boldsymbol{\sigma}}}{\partial \xi} & \frac{\partial \Im}{\partial \hat{\boldsymbol{\sigma}}}\frac{\partial \overline{\boldsymbol{\sigma}}}{\partial \lambda_2} \\ \frac{\partial X}{\partial \hat{\boldsymbol{\sigma}}}\frac{\partial \overline{\boldsymbol{\sigma}}}{\partial \xi} + \frac{\partial X}{\partial \xi} & \frac{\partial X}{\partial \hat{\boldsymbol{\sigma}}}\frac{\partial \overline{\boldsymbol{\sigma}}}{\partial \lambda_2} + \frac{\partial X}{\partial \lambda_2} \end{bmatrix} \begin{bmatrix} \delta\xi \\ \delta\lambda_2 \end{bmatrix} = \begin{bmatrix} -\Im \\ -X \end{bmatrix}$$

4.7.6 Update the unknowns:

$$\xi = \xi + \delta\xi$$

$$\lambda_2 = \lambda_2 + \delta\lambda_2$$

$$\lambda_1 = \lambda_2 / (\alpha_{p2}(1+p))$$

4.7.7 Compute the principal stresses:

$$\hat{\boldsymbol{\sigma}} = \omega\xi\hat{\boldsymbol{\sigma}}^* + \frac{\xi}{3 - 2\tilde{\nu}(1-\xi)}\{\tilde{\nu}(1-\xi)\omega I_1^* - 9(1-d)\tilde{K}_0\lambda_2\}\mathbf{I}$$

4.7.8 Go to Step 4.7.1

4.8 Compute the principal values of the plastic strain increment:

$$\Delta\hat{\boldsymbol{\varepsilon}}^p = \lambda_1 \frac{3}{2\sqrt{3J_2}}(\hat{\boldsymbol{\sigma}} - \frac{I_1}{3}\mathbf{I}) + \lambda_2\mathbf{I}$$

4.9 Go to Step 4.3

4.10 Compute the stress and the plastic strain:

$$\boldsymbol{\sigma} = \mathbf{P}\hat{\boldsymbol{\sigma}}\mathbf{P}^T$$

$$\boldsymbol{\varepsilon}^p_{n+1} = \boldsymbol{\varepsilon}^p_n + \mathbf{P}\Delta\hat{\boldsymbol{\varepsilon}}^p\mathbf{P}^T$$

4.11 Compute the algorithmic tangent stiffness matrix:

$$\left.\frac{d\boldsymbol{\sigma}}{d\boldsymbol{\varepsilon}}\right|_{n+1} = [\mathbf{D}^{-1} + \{\frac{1}{(1-d_p)}\frac{\partial d_p}{\partial \kappa}(\boldsymbol{\varepsilon} - \boldsymbol{\varepsilon}^p)\mathbf{T}_{\kappa\sigma} + \mathbf{V}_{\varepsilon\lambda}\mathbf{T}_{\lambda\sigma} + \mathbf{M}_{\sigma\varepsilon}\}\frac{\partial \hat{\boldsymbol{\sigma}}}{\partial \boldsymbol{\sigma}} + \lambda_1\frac{\partial \tilde{\mathbf{g}}}{\partial \boldsymbol{\sigma}}]^{-1}$$

$$\{\mathbf{I} - \frac{1}{(1-d_e)}(\boldsymbol{\varepsilon} - \boldsymbol{\varepsilon}^p)\frac{\partial d_e}{\partial \boldsymbol{\varepsilon}}\}$$

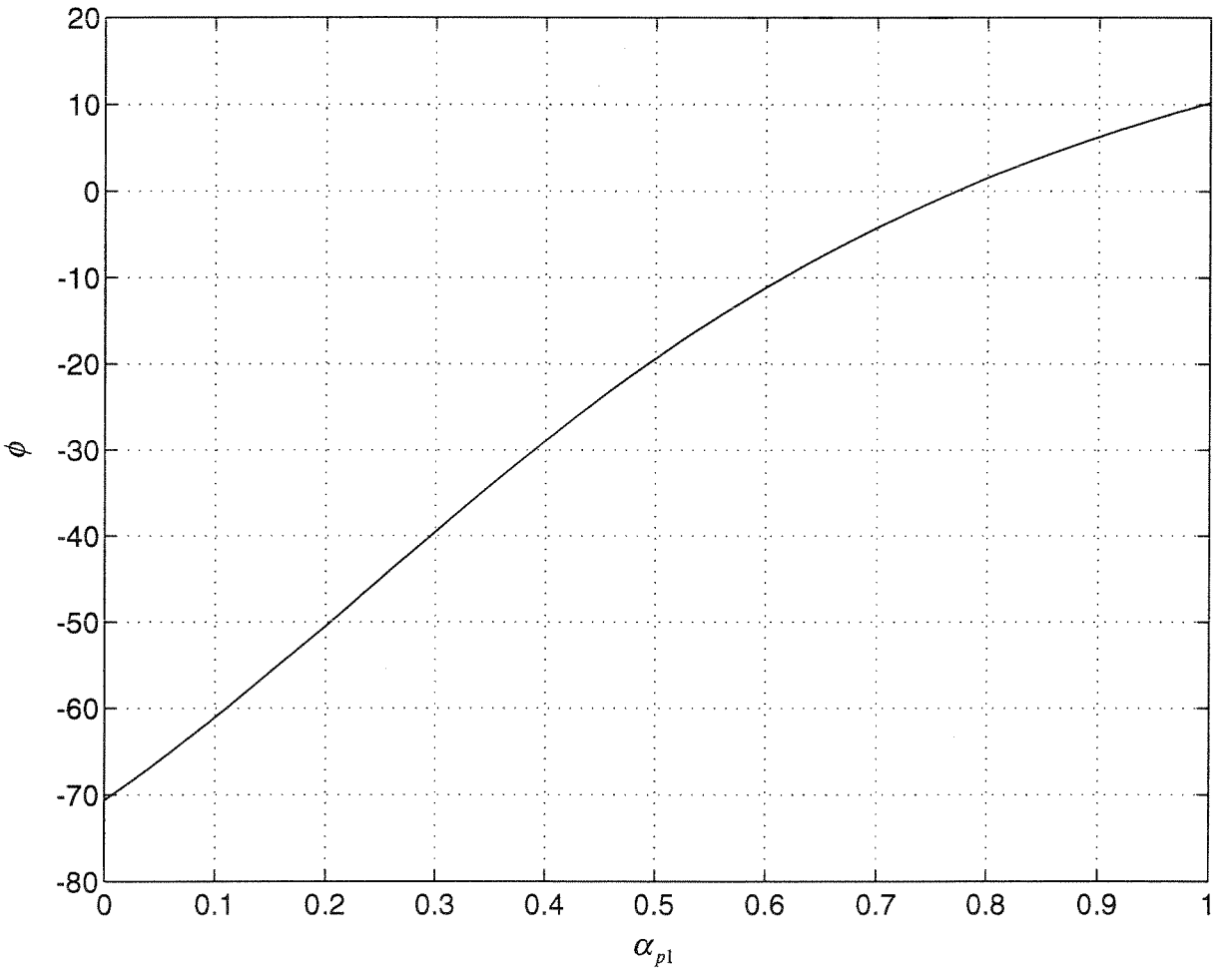

Fig. 3.1 Angle Deciding Boundary (ϕ) - α_{p1} Curve (ν=0.18)

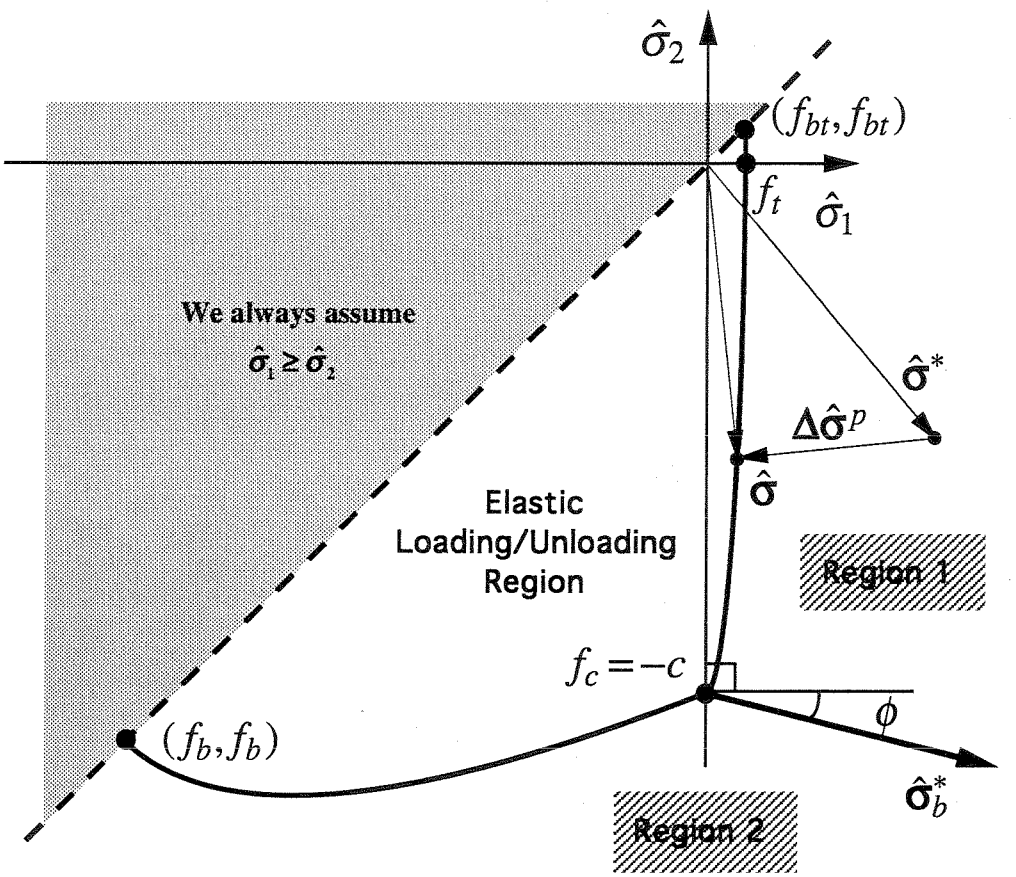

Fig. 3.2 Geometric Interpretation of Two Regions in Principal Stress Plane

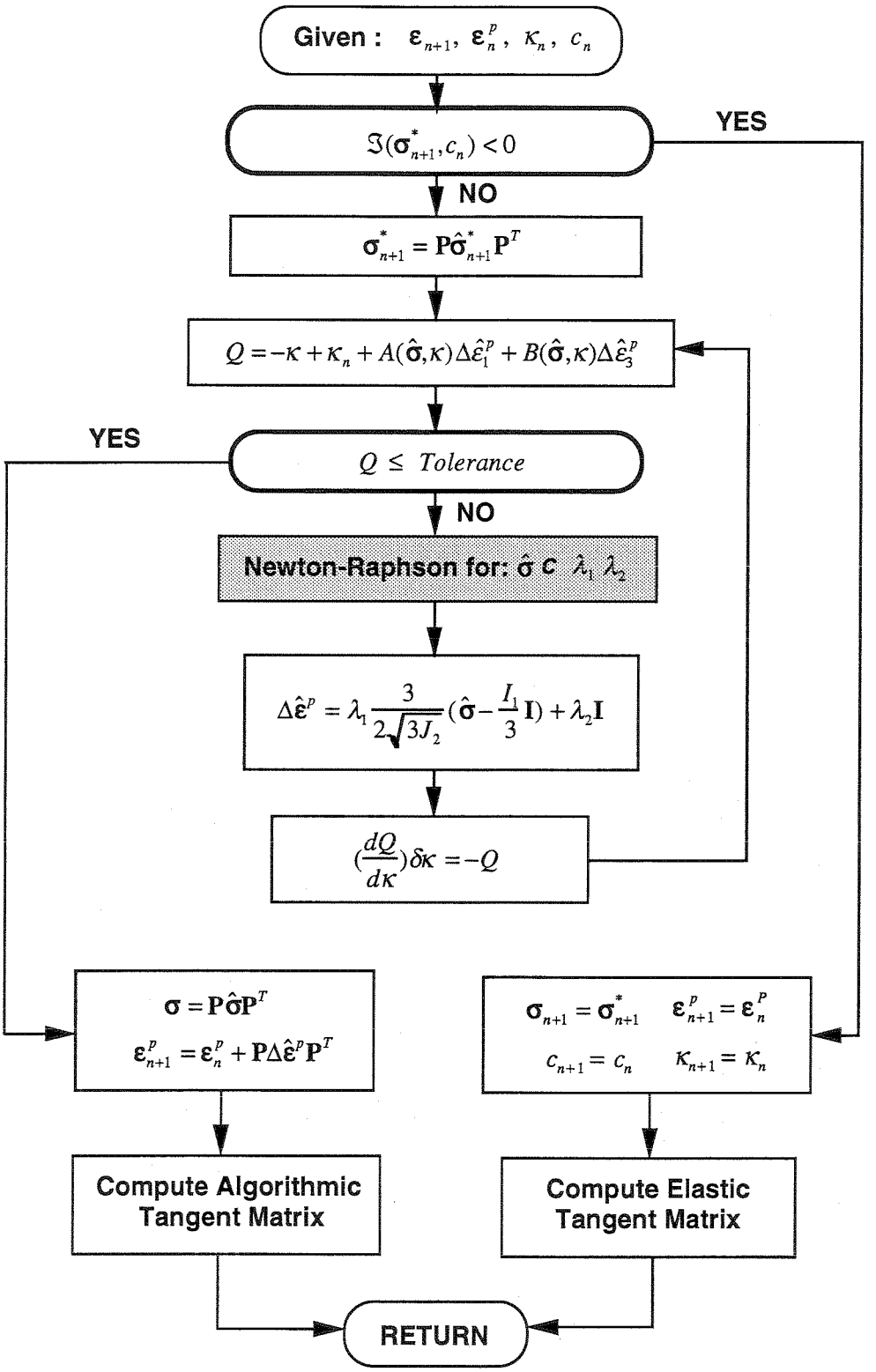

Fig. 3.3 Flow Chart of Plane Stress Algorithm

Chapter 4

APPLICATIONS

4.1 Introduction

The numerical algorithm which has been described in the previous chapter is implemented as a part of the finite element program FEAP [Taylor, 1993]. Users can link their own finite element libraries to the existing FEAP program, which is used mainly for solving the system of nonlinear equations. The numerical algorithm is implemented as a material modeling module, which is called from the element library. The numerical examples in this chapter have been solved by FEAP with the two-dimensional plane quadrilateral isoparametric element.

To demonstrate the performance of the implemented numerical model, the results from four problems are presented in this chapter. The first test verifies the basic capabilities of the model in representing uniaxial tensile and compressive behavior of concrete. By comparing the numerical results from this problem with the experimental ones, we can calibrate the material parameters. Three cyclic-loading cases, uniaxial tensile, uniaxial compressive and tensile-compressive cyclic loading, are carried out in the second test to check how well the model simulates the material behavior in both tensile and compressive regions. The mesh-objectivity is verified by the third test problem. The concept of the characteristic length is applied so that the results are objective to the mesh size.

While the first three tests consist of patch-test style problems, the last test is a numerical example of a cantilever beam to model an idealized dam. The beam is subjected to the cyclic loading that can be interpreted as the quasi-static loading.

The plane stress is assumed in the following numerical test problems. All external loads have been imposed by displacement control. The following material properties and the model parameters are used for all numerical tests:

$$f_{cy} = \text{-2800 psi}, \quad f_c' = \text{-4000 psi}, \quad f_{by} = \text{-3300 psi}, \quad \nu = 0.18,$$
$$\alpha_{p1} = 0.5, \quad \alpha_{p2} = 0.1, \quad \text{m} = 1.5, \quad a_t = 0.1$$

The other material properties and parameters of the model are described in each section.

4.2 Monotonic Loading Tests

In order to compare the numerical results with the existing experimental results [Karsan and Jirsa, 1969; Gopalaratnam and Shah, 1985], the following material properties and the model parameters are used in each case:

1) Monotonic tensile loading:

$E = 4.8\times10^6$ psi, $f_t' = 500$ psi, $\varepsilon_u = -0.001$, $d_u = 0.2$,
$G_t = 0.08$ lb/inch, $l = 1$ inch

2) Monotonic compressive loading:

$E = 4.5\times10^6$ psi, $f_t' = 500$ psi, $\varepsilon_u = -0.001$, $d_u = 0.02$,
$G_c = 17$ lb/inch, $l = 1$ inch

The single-element patch shown in Fig. 4.1(a) has been used for these tests. Only uniaxial load has been applied in the monotonic loading tests.

The objectives of the monotonic loading tests are:

1) To evaluate the performance of the developed numerical model for the fundamental and simple loading situations,
2) To carry out the patch test in the context of the finite element method,
3) To calibrate the parameters which are used to generate the appropriate elastic and plastic stiffness degradation.

Fig. 4.2 and Fig. 4.3 show the resulting tensile and compressive stress-strain curves, respectively. The curves calculated by the implemented algorithm agree well with the experimental data. The evolution of damage variable under the monotonic tensile loading is given in Fig. 4.4.

In Fig. 4.2, the experimental data shows a very steep post-peak curve, since the data were measured by the wide strain gage over the localized zone. If we consider the stress-strain relation in the localized zone, the absolute value of the negative tangential stiffness after the ultimate stress point will decrease. The numerical model cannot yield the large softening stiffness, not only because the stress curve shape is based on the difference of two exponential curves [Lubliner, et al., 1989], but because there is the fundamental limitation in establishing the initial boundary problems for softening materials. In uniaxial problems without the degradation of stiffness, the absolute value of negative stiffness

representing softening behavior should be less than the elastic secant stiffness [Simo and et al., 1988].

Granual materials, such as soil, rock and concrete, are known to give a significant volume change which is caused by the large amount of the inelastic strain. An increasing volume change, called dilatancy, is observed in the specimen subjected to uniaxial compressive loading. The dilatancy can be modeled in the numerical model and the results are shown in Fig. 4.5. It is noted that the amount of dilatancy is decided by α_{p1}.

4.3 Cyclic Loading Tests

In this section, the results from three uniaxial cyclic loading cases present. The same finite element model as in Section 4.2 is used. The first case has been performed for cyclic tensile loading with the material properties and the model parameters:

$E = 4.8\times10^6$ psi, $f_t' = 500$ psi, ε_u = -0.001, $d_u = 0.2$,
$G_t = 0.08$ lb/inch, $G_c = 14$ lb/inch, $l = 1$ inch

The comparison with the experimental data [Gopalaratnam and Shah, 1985] is illustrated in Fig. 4.6. The degradation of the stiffness is seen to be properly simulated. Again, the smaller absolute value of the stiffness of the numerical result in the softening branch than that of the experimental one can be explained by the same notion given in the previous section.

The second case has been done for compressive cyclic loading with:

$E = 3.8\times10^6$ psi, $f_t' = 500$ psi, ε_u = -0.001, $d_u = 0.02$,
$G_t = 0.08$ lb/inch, $G_c = 14$ lb/inch, $l = 1$ inch

Fig. 4.7 shows the numerical result compared with the experimental one [Karsan and Jirsa, 1969].

The last case for the cyclic loading is the model subjected to cyclic tensile-compressive load. The material properties and the model parameters are used in order that we can compare the numerical results with the different experimental results [Reinhart, 1984]:

$E = 3.3\times10^7$ psi, $f_t' = 500$ psi, ε_u = -0.0001, $d_u = 0.5$,
$G_t = 0.04$ lb/inch, $G_c = 8$ lb/inch, $l = 1$ inch

In Fig. 4.8, we can see good numerical results for the full-cyclic behavior of concrete. The microcrack opening and closing are simulated by the elastic degradation which is proportional to the recoverable tensile strain. The limitation in modeling the crack opening and closing is due to the fact that the continuum model is used to simulate the discrete phenomenon (that is, the contact problem). But, this limitation is inevitable in that the model should be as simple as possible to handle the problems having many cyclic loading steps and degrees of freedom.

4.4 Mesh-Sensitivity Tests

The sensitivity to mesh size has been analyzed to check the mesh-objectivity which is expected to be obtained by using the mesh-dependent characteristic length [Lubliner and et al., 1989]. Three problems having the same specimen dimensions but different mesh sizes were tested to check the sensitivity to mesh size. Each mesh and boundary condition is illustrated in Fig. 4.1. To make the strain localization occur at the left-end element consistently, the perturbation using less tensile strength was imposed to the element. The material properties and model parameters which are used in all mesh types are:

$E = 4.8 \times 10^6$ psi, $f_t' = 500$ psi, $\varepsilon_u = -0.001$, $d_u = 0.1$
$G_t = 0.075$ lb/inch, $G_c = 7.5$ lb/inch

The fracture energies are scaled by the characteristic length, l, that equals the mesh size in the horizontal direction:

1) Mesh B: $l = 1$ inch
2) Mesh C: $l = 0.5$ inch
3) Mesh D: $l = 0.25$ inch

Fig. 4.9 shows the resulting load-displacement curves which have been measured at the end of the specimens. While the left-end element is undergoing strain localization, the other elements, if any, are in an elastic unloading state after the ultimate strength point. Since the softening by the plastic-damage evolution is not linear, the three curves cannot be exactly identical regardless of the numerical error. Nevertheless, the global post-peak behaviors are similar to one another and to the stress-strain relation (Fig. 4.10) which is

assumed as the unique material property in the model. Fig. 4.11 shows that the strain is localized in the left-end element as expected.

4.5 Cyclic-Loaded Cantilever Beam Test

As the final example, a rectangular cantilever beam subjected to cyclic loading is presented. At the free end, the prescribed cyclic displacement is imposed to simulate the elastoplastic behavior with the elastic and plastic damage evolution of the beam under quasi-static loading. The configuration of the mesh is illustrated in Fig. 4.12. The stability, existency and uniqueness of the solution at the structural level and material level are assumed to be maintained in this example. The following material properties and model parameters are used:

$E = 4.0 \times 10^6$ psi, $f_t' = 450$ psi, $\varepsilon_u = -0.001$, $d_u = 0.02$,
$G_t = 0.25$ lb/inch, $G_c = 25$ lb/inch, $l = 0.5$ inch

where the characteristic length, l, equals the mesh size of the left-end elements in the horizontal direction, since the microcracks are assumed to be propagated along the vertical direction of the beam.

The cyclic response of load-displacement relation at the free end is shown in Fig. 4.13. In first two cycles, the maximum prescribed displacement equals 0.0049 inch and after that, in two more cycles, 0.0045 inch is prescribed. The last cycle was not completed since the beam almost collapsed and therefore, the numerical model also enters an the unstable state. The step-by-step damage propagation is illustrated in Fig. 4.14. As the number of loading cycles increases, the resulting pattern of the damage propagation becomes parallel in the vertical direction, which is observed in an unreinforced cantilever beam having significantly developed microcracks. The displacement contours after two and three-quarter cycles are given in Fig. 4.15, where the strain localization is clearly appearing. Fig. 4.16 shows the stress components after two and three-quarter cycles.

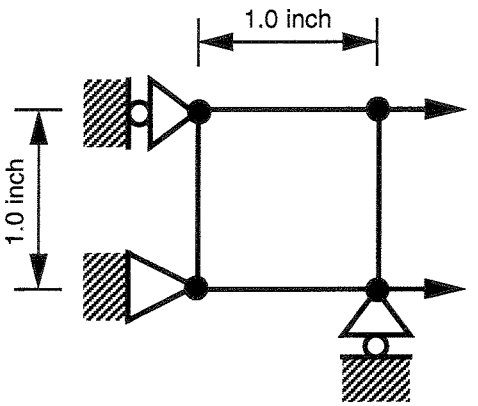

(a) Mesh A

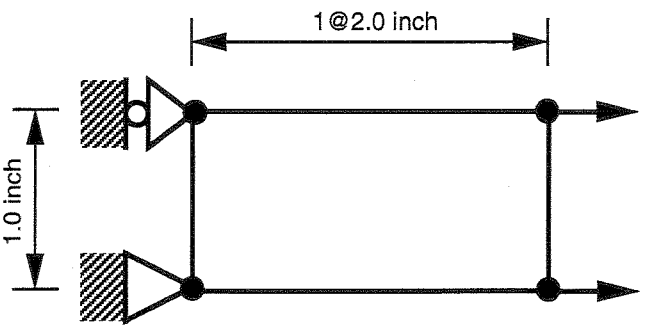

(b) Mesh B

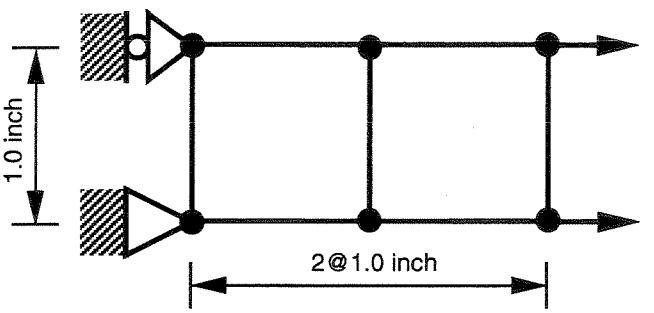

(c) Mesh C

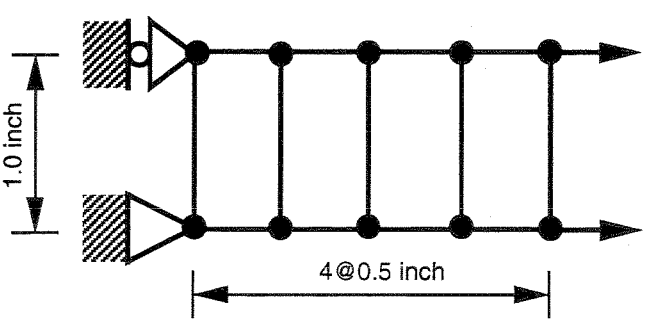

(d) Mesh D

Fig. 4.1 Finite Element Meshes for Test Examples

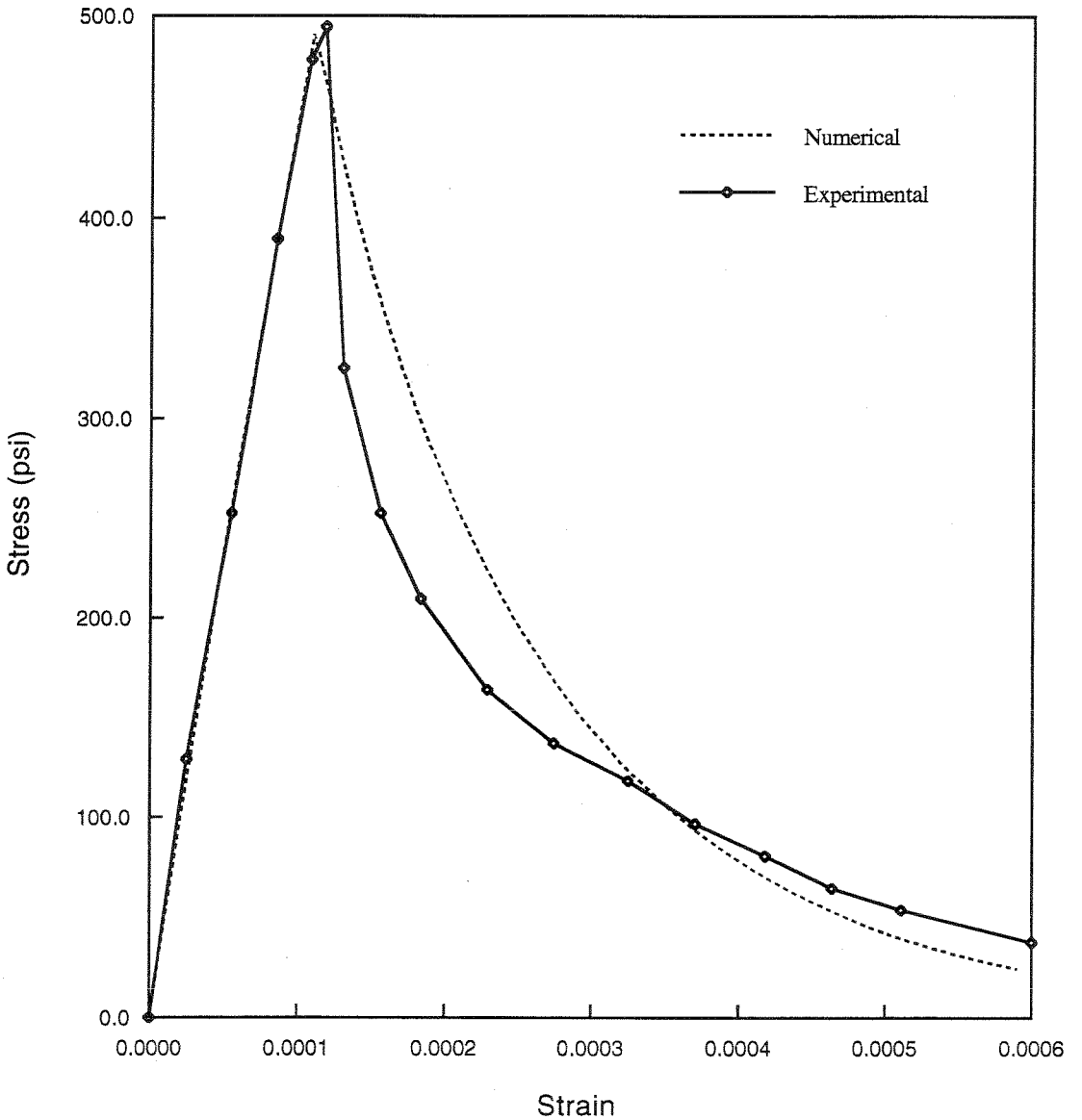

Fig. 4.2 Monotonic Tensile Loading Case

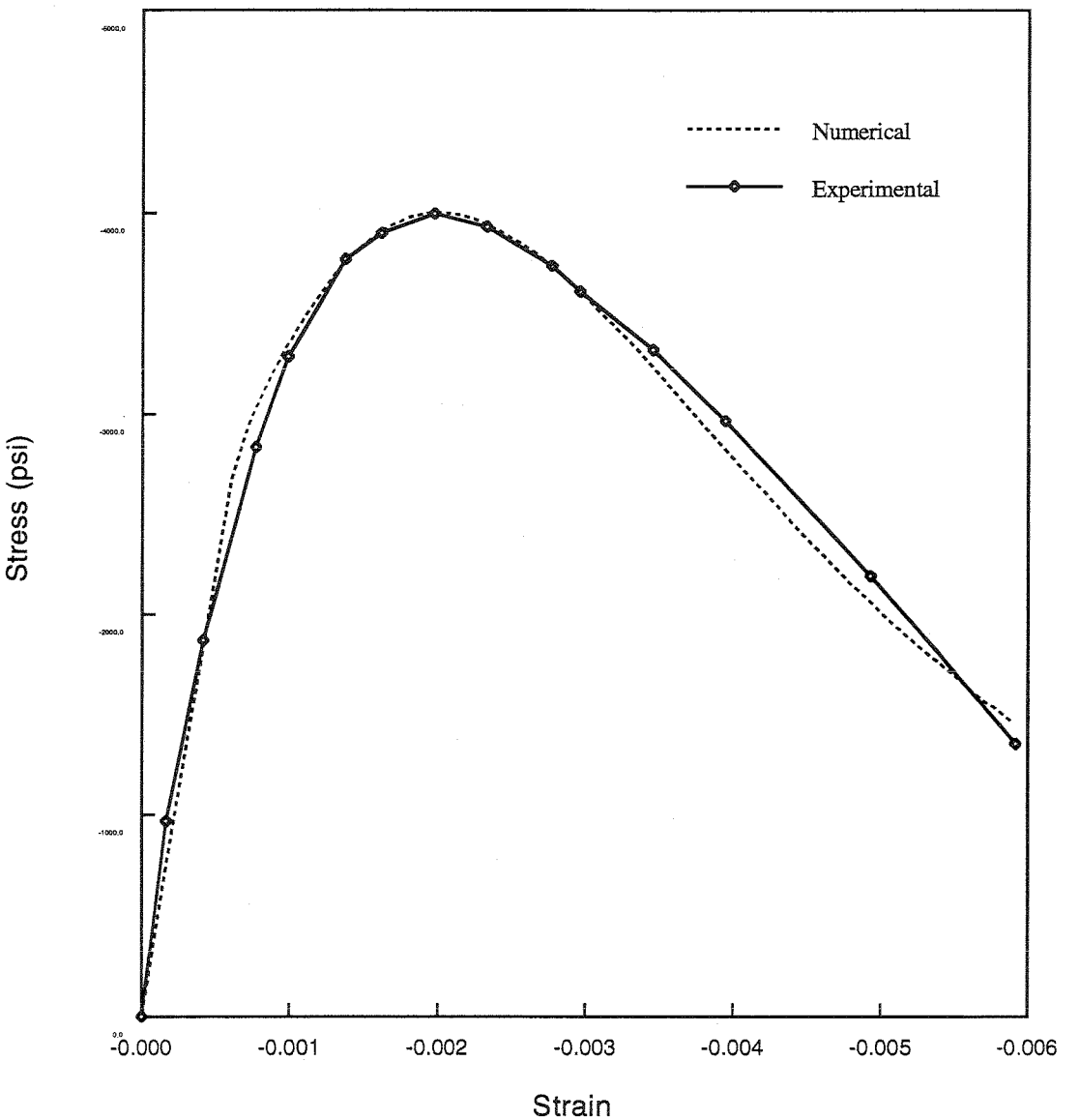

Fig. 4.3 Monotonic Compressive Loading Case

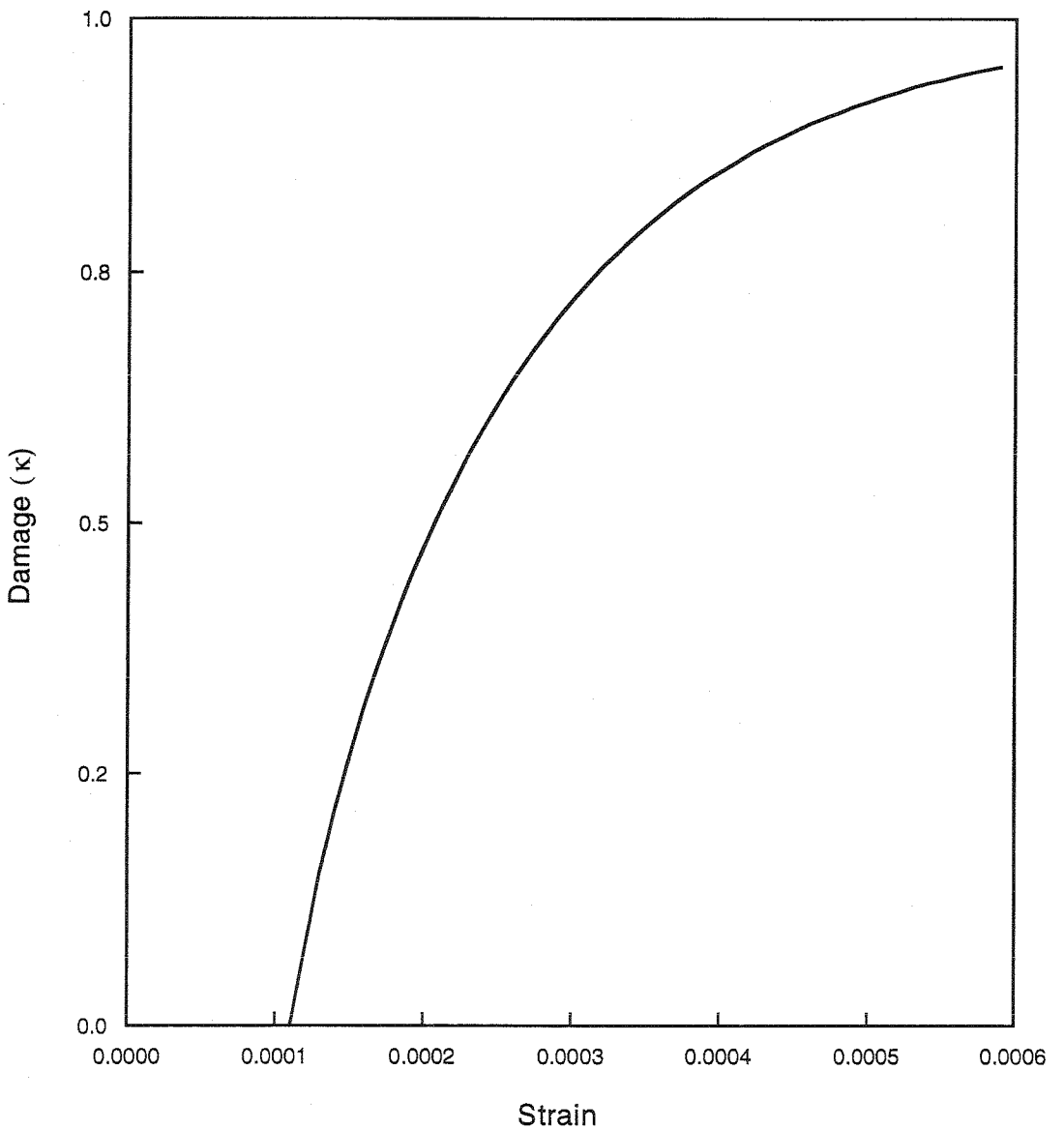

Fig. 4.4 Damage Evolution under Monotonic Tensile Loading

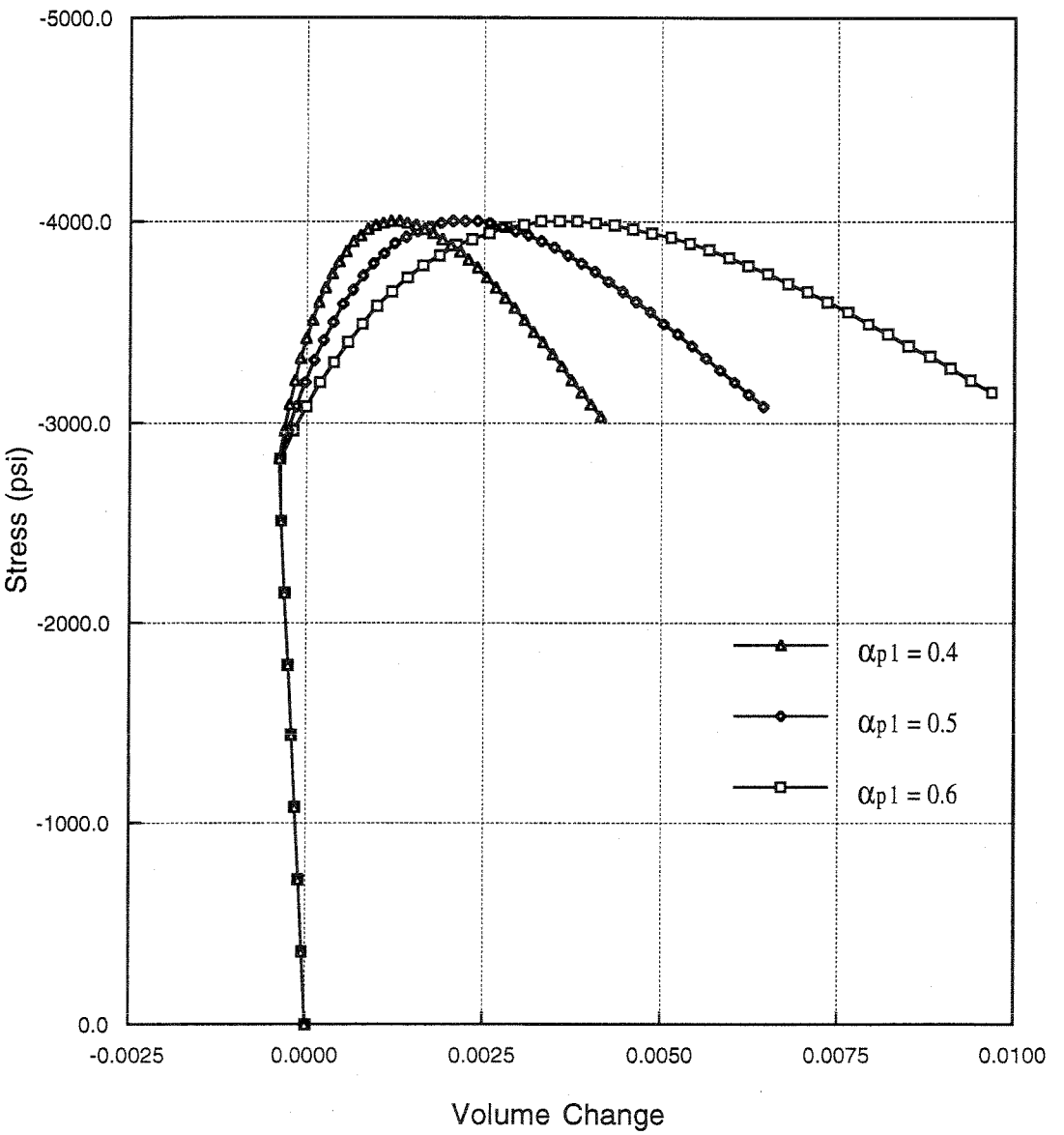

Fig. 4.5 Uniaxial Compressive Stress-Volume Change Curves

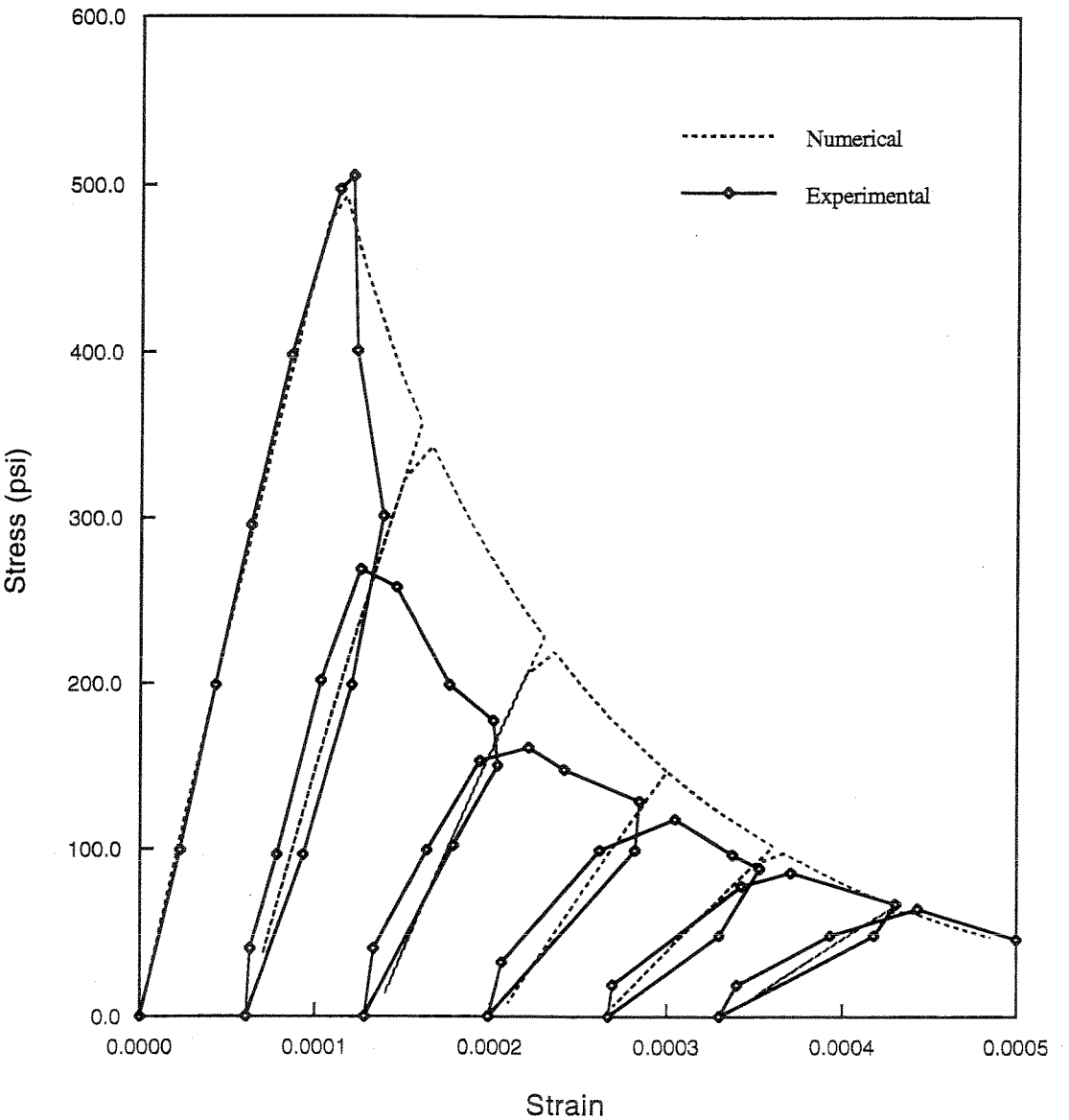

Fig. 4.6 Cyclic Tensile Loading Case

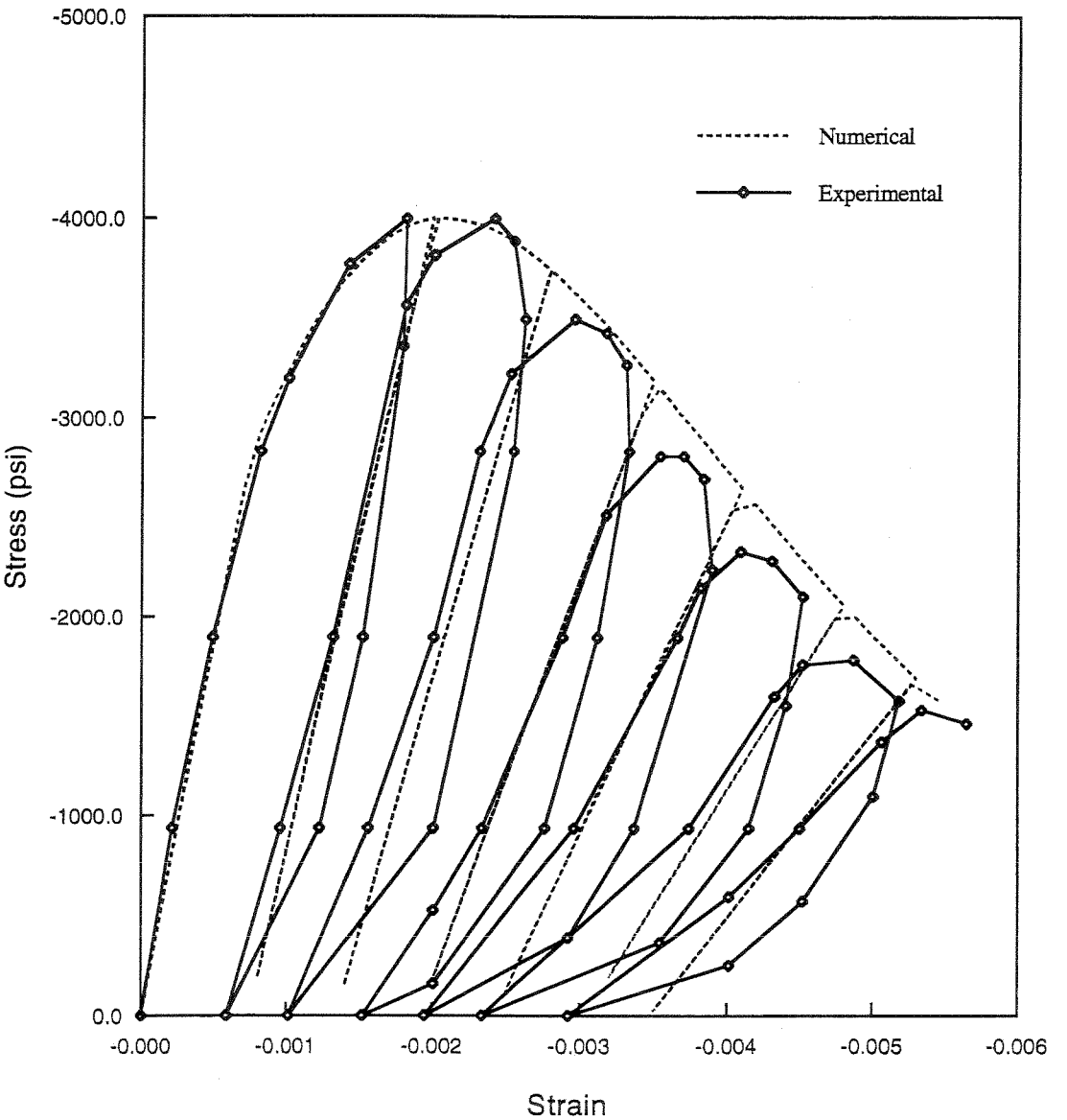

Fig. 4.7 Cyclic Compressive Loading Case

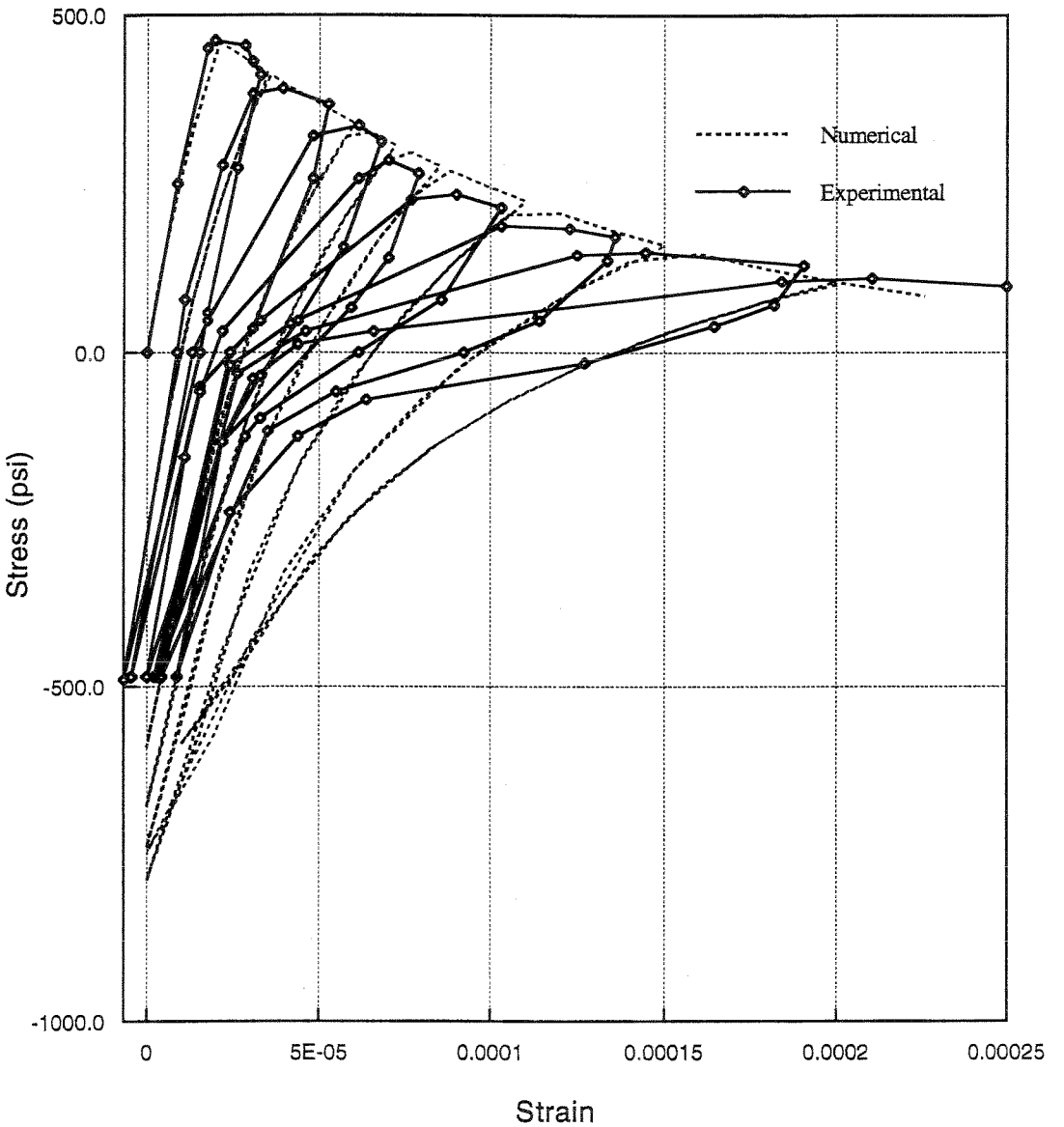

Fig. 4.8 Cyclic Tensile-High Compressive Loading Case

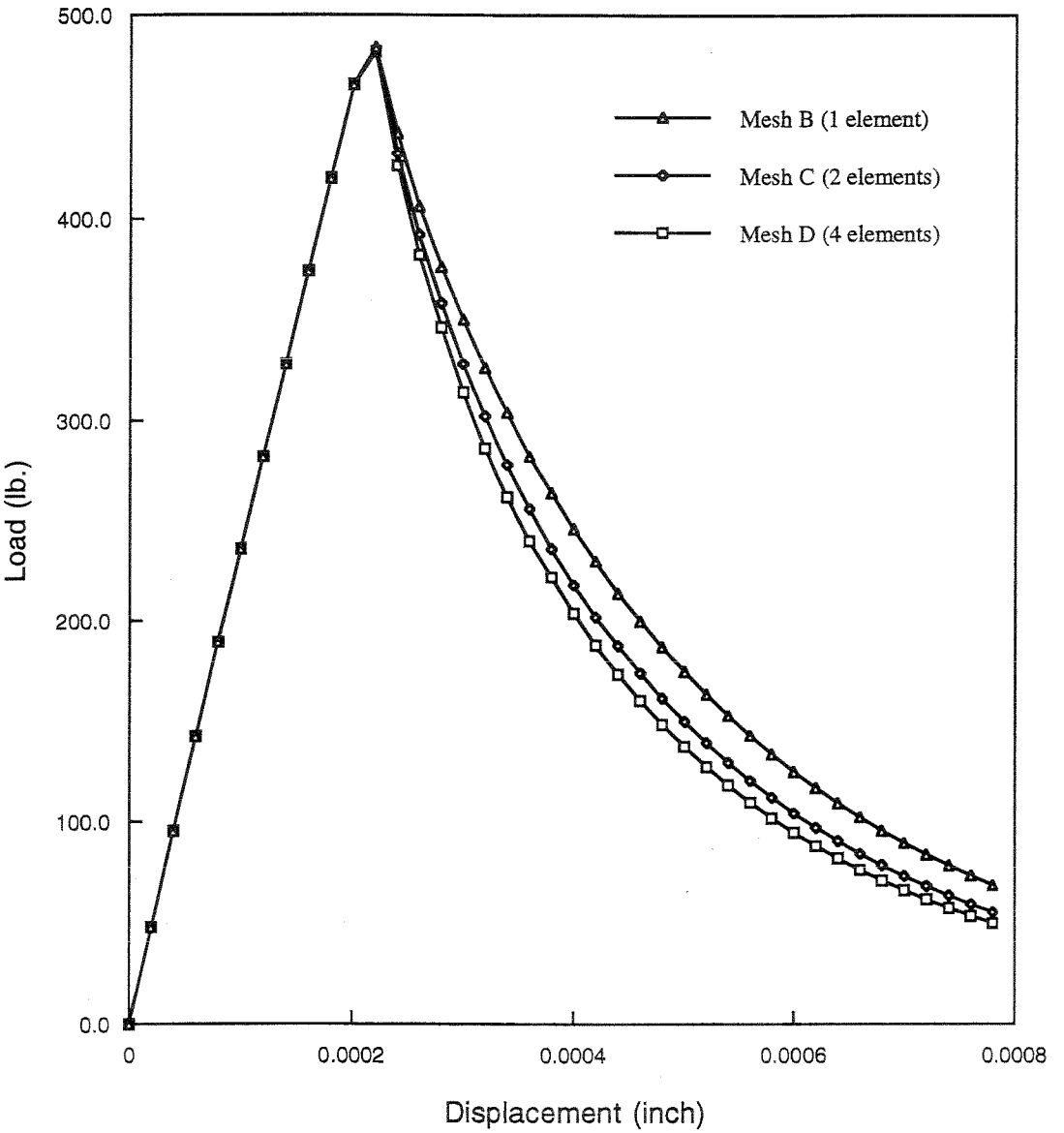

Fig. 4.9 Load-Displacement Curves from Different Mesh Sizes

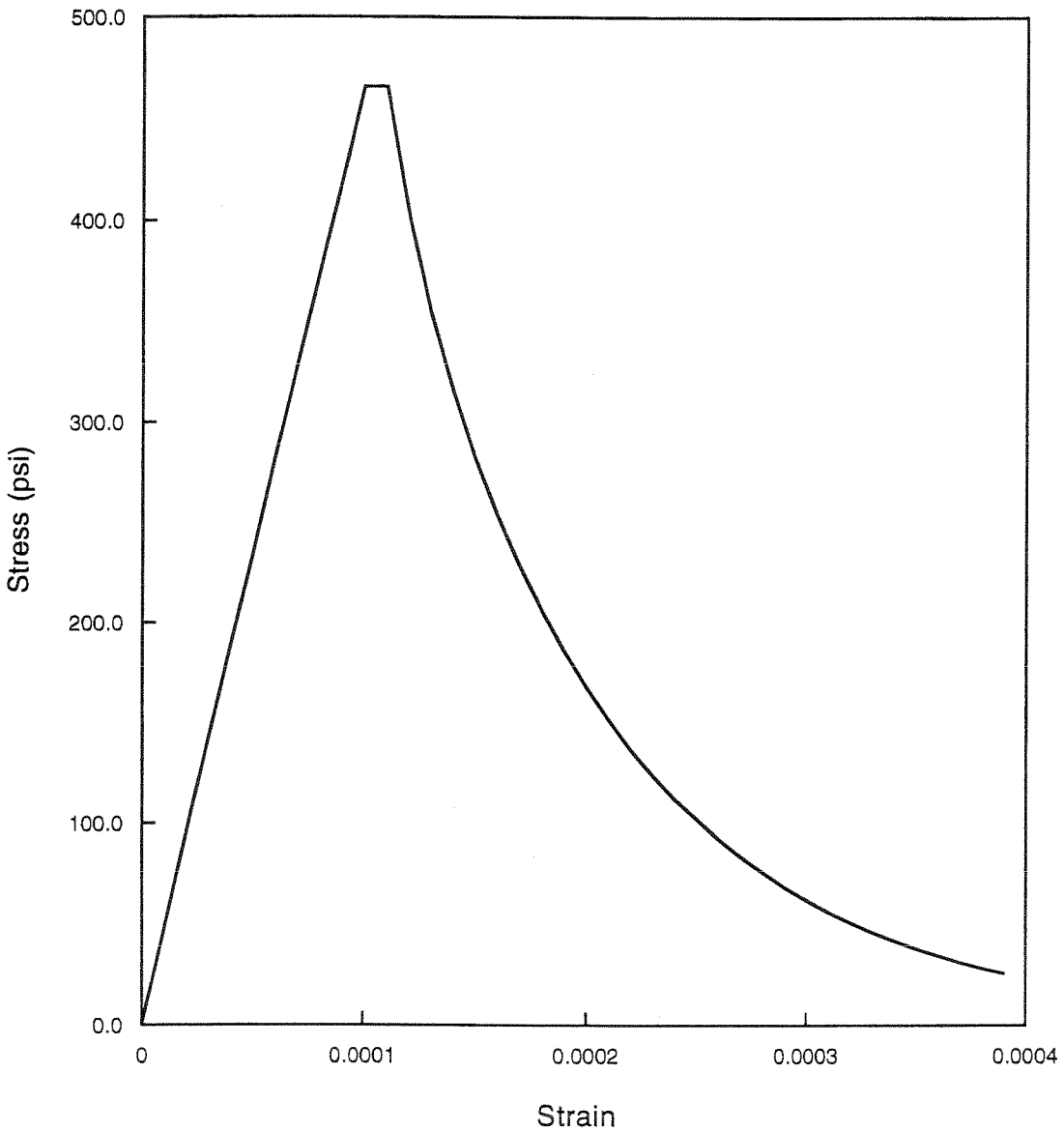

Fig. 4.10 Stress-Strain Relation for Mesh-Sensitivity Analysis

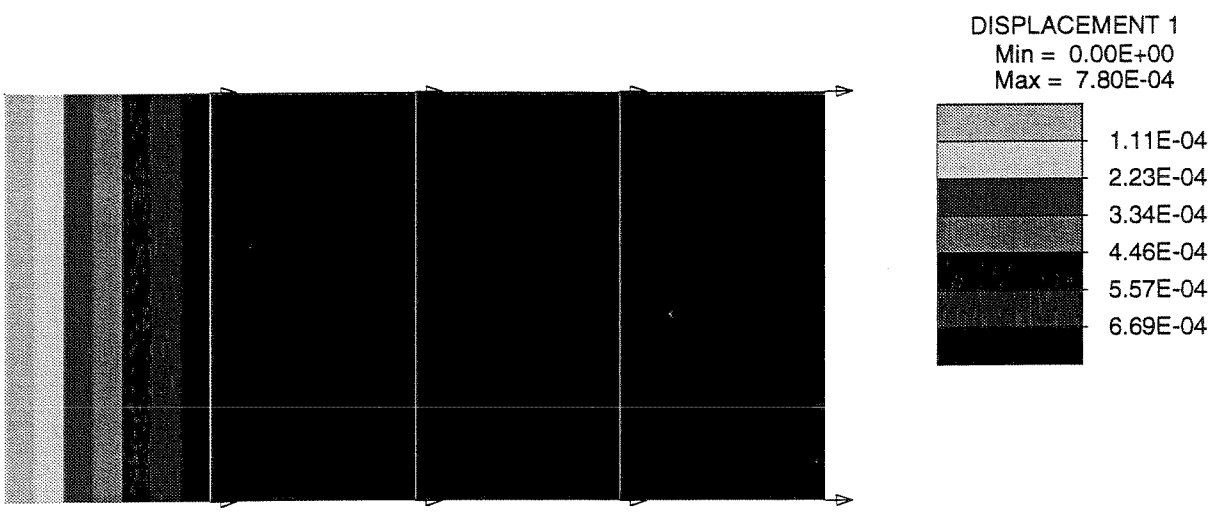

Fig. 4.11 Displacement Contour for Mesh D in Mesh-Sensitivity Analysis

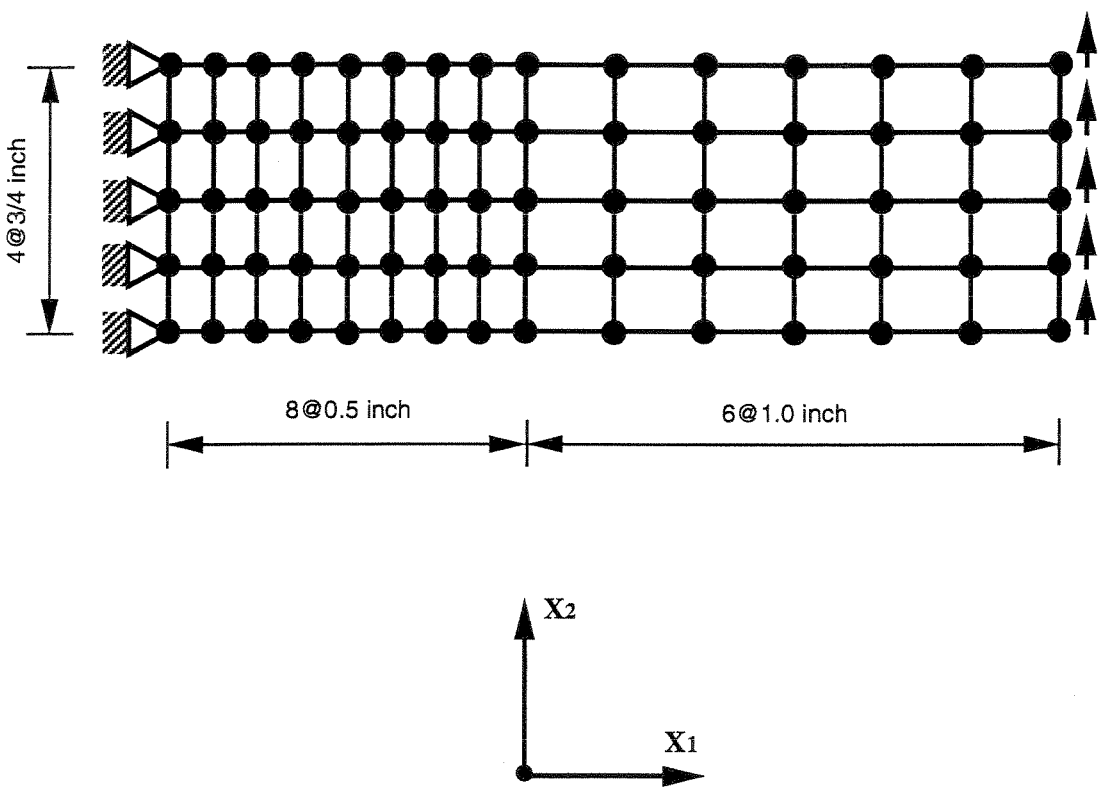

Fig. 4.12 Finite Element Mesh for Cantilever Beam Example

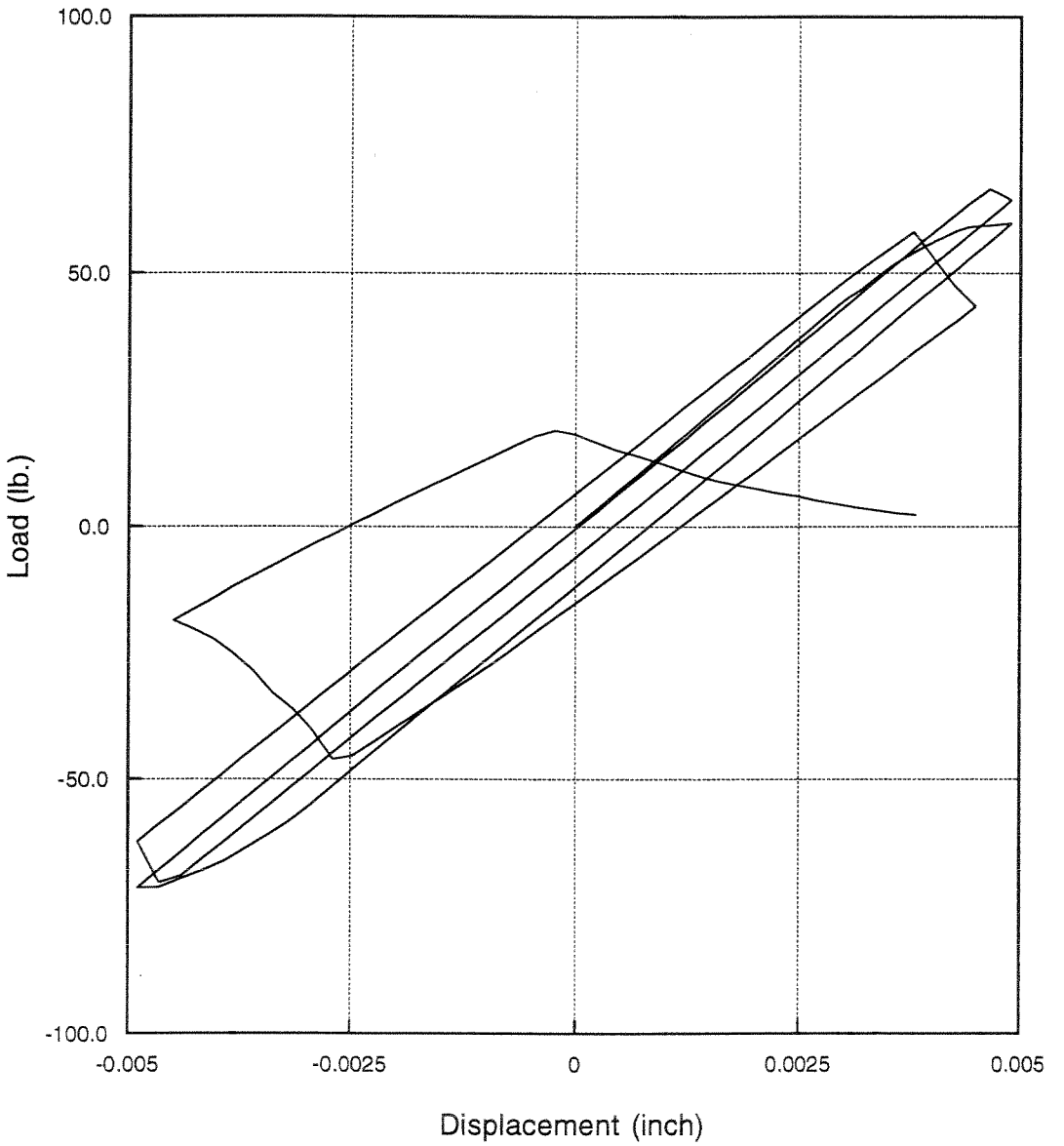

Fig. 4.13 Cantilever Beam under Cyclic Loading

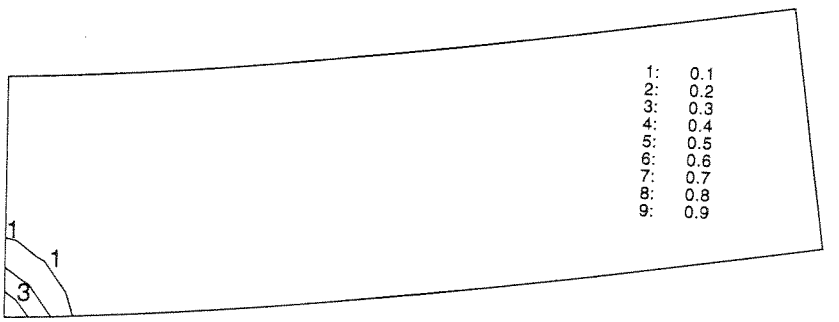

(a) After One-Quarter Cycle

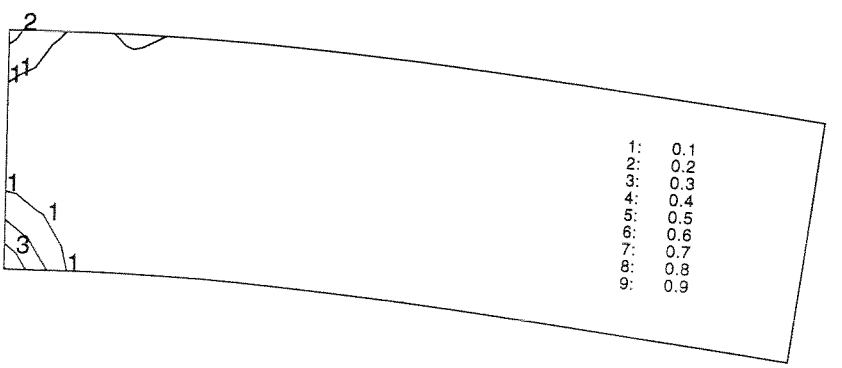

(b) After Three-Quarter Cycles

Fig. 4.14 Damage Evolution of Cantilever Beam under Cyclic Loading

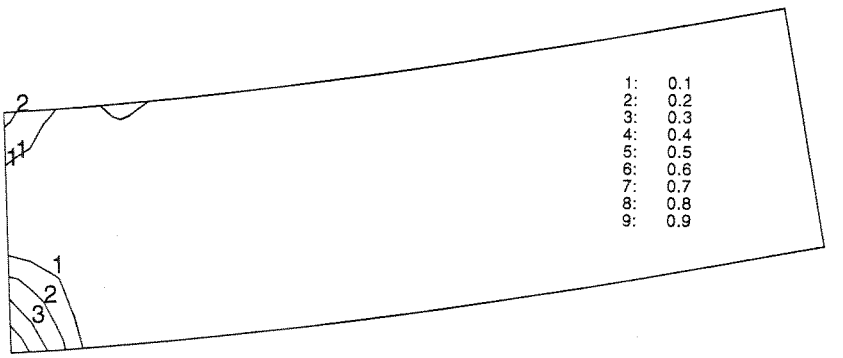

(c) After One and One-Quarter Cycles

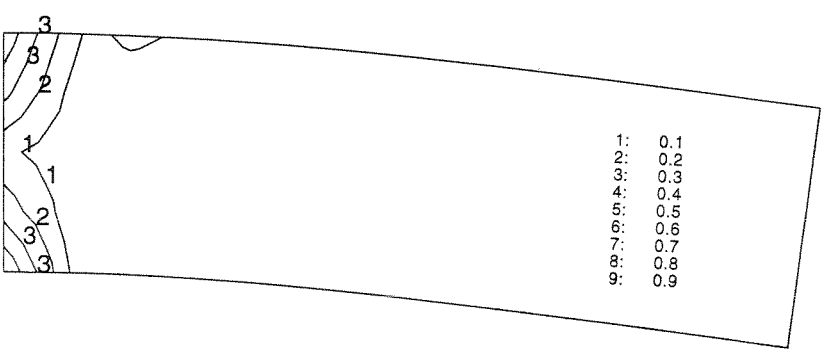

(d) After One and Three-Quarter Cycles

Fig. 4.14 Damage Evolution of Cantilever Beam under Cyclic Loading (Continued)

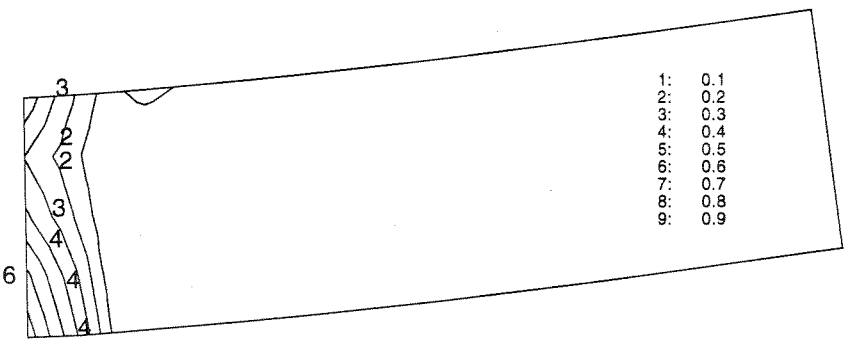

(e) After Two and One-Quarter Cycles

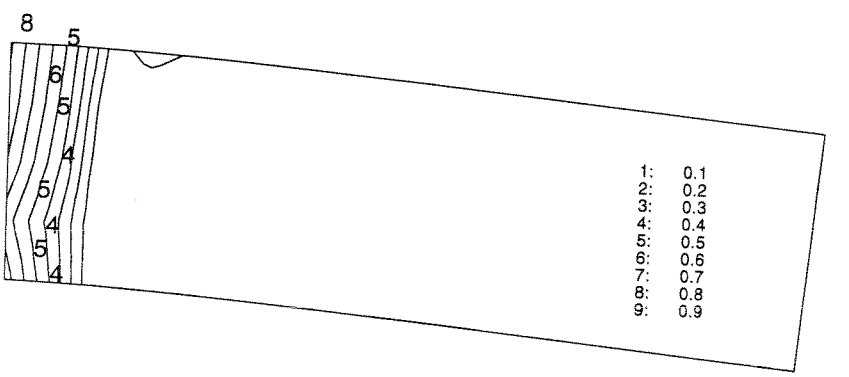

(f) After Two and Three-Quarter Cycles

Fig. 4.14 Damage Evolution of Cantilever Beam under Cyclic Loading (Continued)

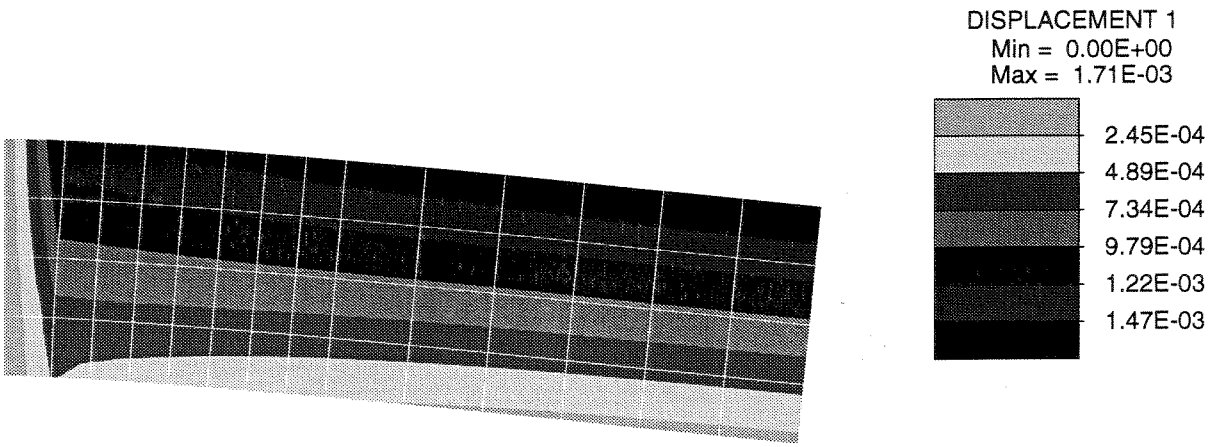

(a) u_1 Component

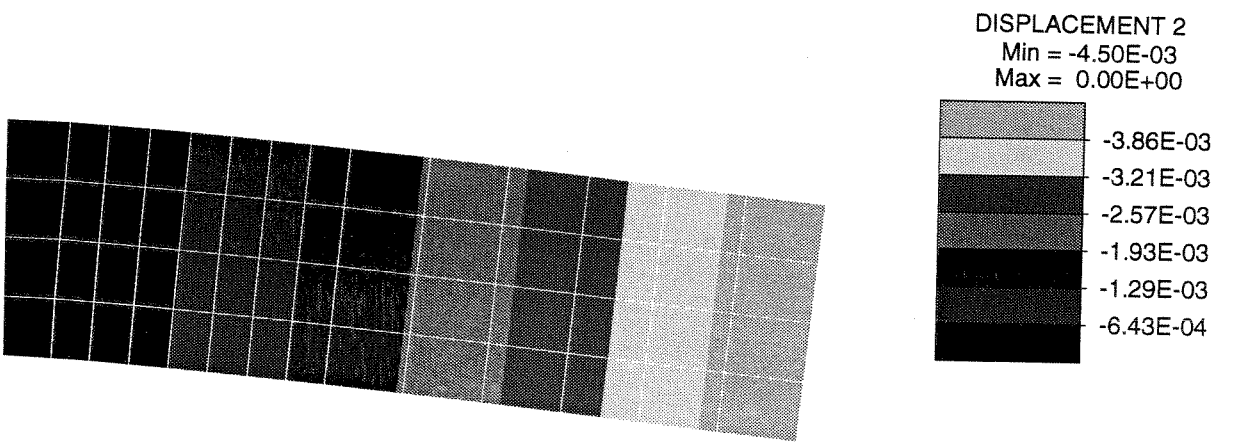

(b) u_2 Component

Fig. 4.15 Displacement Contours for Cantilever Beam (After Two and Three-Quarter Cycles)

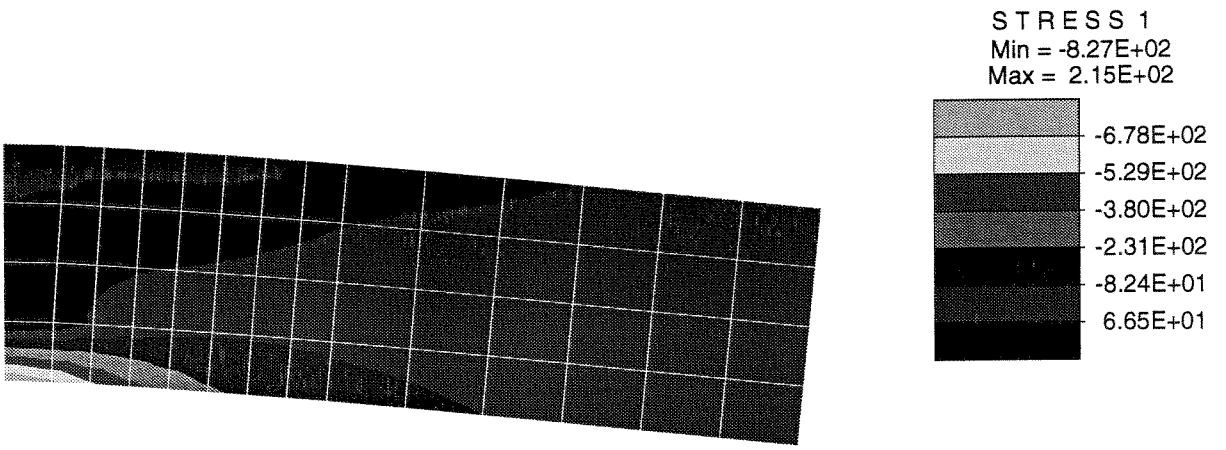

(a) σ_{11} Component

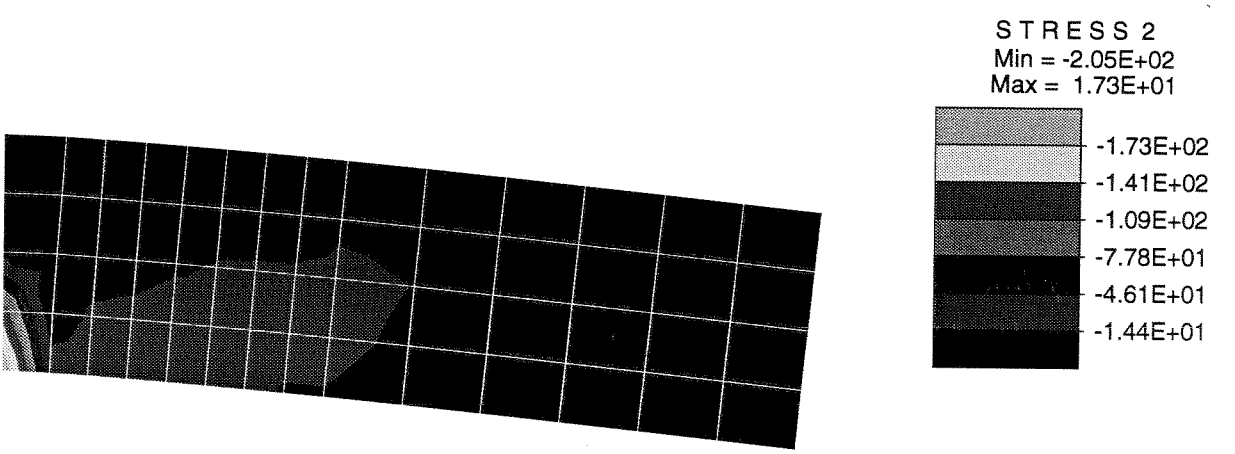

(b) σ_{22} Component

Fig. 4.16 Stress Contours for Cantilever Beam (After Two and Three-Quarter Cycles)

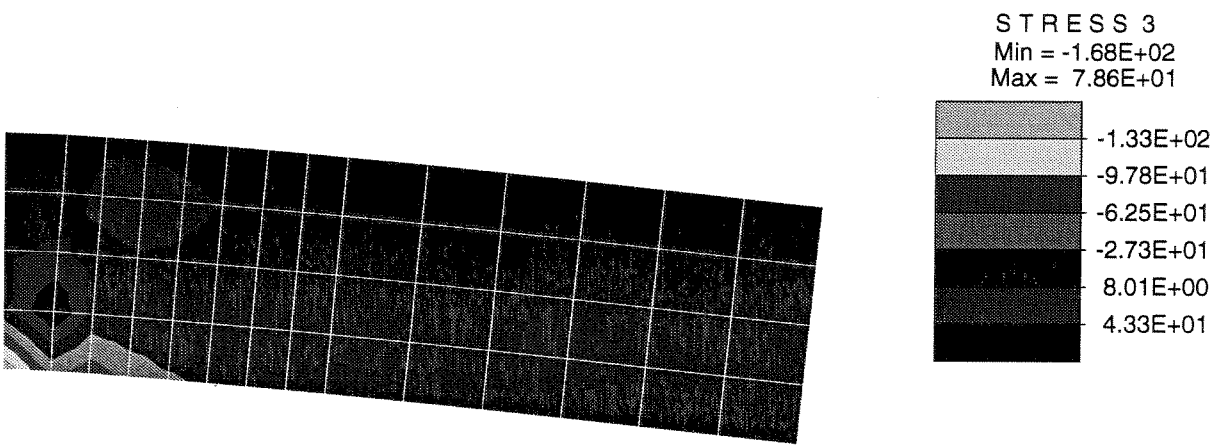

(c) σ_{12} Component

Fig. 4.16 Stress Contours for Cantilever Beam (Continued)

Chapter 5

CONCLUSIONS

In this study, a new numerical scheme has been presented to implement a plastic-damage model, which is modified from Lubliner's constitutive model for both the softening and hardening behavior of concrete material. The new algorithm is derived from the standard return-map scheme by using the spectral decomposition of stresses.

It is shown that Lubliner's yield function simulates the real behavior of concrete for both tensile and compressive loading under cyclic loading. To model the significant volume change from the inelastic strains, the non-associative flow rule is necessary. The non-associative flow rule generated from the multiple plastic potential functions are used to avoid the corner zones on the yield surface, which give singular gradient vectors of the yield function. This flow rule is less general than the multi-surface plasticity, but it allows a simpler numerical solution and still gives good results as shown in the study. The scalar elastic degradation and plastic degradation variables, which are similar to the damage variables in continuum damage mechanics, are used to simulate the degradation of the elastic secant stiffness. Modeling the degradation is very important for cyclic loading problems. The elastic degradation is related to the total strain to represent the crack opening/closing. Plastic damage is included in the model to obtain more degradation, which is observed in the softening zone. It is noted that the elastic degradation is reversible while the plastic degradation is not.

The concept of damage variables for modeling both softening and hardening behavior by one scalar damage evolution rule gives a simple approach for simulating the concrete behavior under cyclic loading. Though a more complicated damage rule could give more realistic results, Lubliner's damage rule gives acceptable results in an inexpensive way. Under cyclic loading, the use of an inexpensive as well as accurate model is desirable.

The spectral return-map algorithm is derived after observing the fact that the eigenvectors of the stress matrix are the same as those of the trial stress matrix, which means the eigenvectors of the stress are preserved through the stress computation procedure, which is iterative. This fact leads to a decoupled formulation of the standard return-map algorithm. Each entry of the decoupled matrices corresponds to the eigenvalues of the matrices. The decoupled return-map algorithm gives the following advantages:

1) Because the iteration is performed on the decoupled equations, the procedure becomes simpler and uses less operations.
2) It is not necessary to use a six-dimensional (three-dimensional) vector form for a 3-by-3 (2-by-2) symmetric tensor. Using this form results in a complicated form of tangent matrices, which is required in an iterative scheme for the corrector stage in the return-map algorithm.
3) Developing the algorithm for the plane stress problem is straightforward as described in Section 3.5.1.
4) Repeated computation of the eigenvalues of stresses and plastic strains, which play important roles in the plastic-damage model, is not necessary during the local iteration because the iterative equations consist of the eigenvalues themselves.

Through the numerical examples, the new numerical algorithm for the modified plastic-damage model is shown to give excellent results. These numerical results agree well with the experimental data under cyclic loading as well as monotonic loading. The numerical algorithm using the characteristic length shows mesh-independency. Of course, the results with different meshes are not exactly identical because of the natural nonlinearlities of damage evolution. The crack opening/closing by contact of the cracked free surfaces are simulated approximately. Because the real stiffness recovery is shown immediately after the contact of the cracked surface, the numerical model, based on two or three dimensional elastoplasticity or continuum damage mechanics, has nearly singular elastic secant stiffness, which is not admissible. The beam example shows the performance of the present numerical algorithm in solving a more realistic problem.

During the computation of the examples with the single element, the quadratic convergence rate is obtained as expected while the super-linear convergence rate is shown in the examples with more than one element. The loss of the quadratic convergence starts when the damage evolution states at the quadrature points in one element become different from one another. This situation yields numerical errors in the computation of the tangent stiffness matrix, which results in the loss of the quadratic convergence rate. It is noted that the loss of the quadratic convergence rate does not negate the utility of the algorithmic tangent stiffness, since only linear convergence rate is available without it.

Consequently, the test results show that the numerical implementation of the modified plastic-damage model, based on Lubliner's model, simulates concrete behavior under cyclic loading very well.

The softening behavior produces ill-posed problems, which means uniqueness is not guaranteed. This leads to instability at structural level because the nonlinear solver could

converge to a solution which is not physically meaningful and, consequently, in the next step, the nonlinear system, which has the wrong initial values (the converged solution at the previous step), would not converge. The solution of this problem requires research because it is not clearly understood yet. The instability from the softening phenomenon is related to the boundary-value problem describing the structure, which consists of the softening material. In the present model, plastic degradation of elastic stiffness is coupled with inelastic strains. This coupling may cause an inconsistent iterative state. In other words, the inadmissible plastic unloading state can occur during the iteration in which the plastic loading state is predicted by the trial stress.

The research has shown that the plastic–damage model can accurately represent the cyclic behavior of plain and mass concrete. Future research will concentrate on improving the model to prevent inadmissible plastic unloading states, and integration of the constitutive model with nonlinear, dynamic analysis procedures for the earthquake analysis of concrete dams.

This page is left blank

REFERENCES

Ayari, M. L. and Saouma, V. E. (1990). "A Fracture Mechanics Based Seismic Analysis of Concrete Gravity Dams Using Discrete Cracks," *Engineering Fracture Mechanics*, Vol. 35, No. 1/2/3, pp. 587-598.

Bazant, Z. P. and Oh, B. H. (1983). "Crack Band Theory for Fracture of Concrete," *Materials and Structures* (RILEM, Paris), Vol. 16, pp. 155-177.

Bazant, Z. P. and Oh, B. H. (1984). "Rock Fracture via Strain-softening Finite Elements," *Journal of the Engineering Mechanics Division*, ASCE, Vol. 110, No. 7, pp. 1015-1035.

Borst, R. De, Sluys, L. J., Muhlhaus, H. -B. and Pamin, J. (1993). "Fundamental Issues in Finite Element Analyses of Localization of Deformation," *Engineering Computation*, Vol. 10, pp. 99-121.

Chen, W. F. and Han, D. J. (1988). *Plasticity for Structural Engineers*, Springer-Verlag, NY.

Crisfield, M. A. (1991). *Non-linear Finite Element Analysis of Solids and Structures*, Vol. 1: Essentials, John Wiley and Sons, Chichester.

Dahlblom, O. and Ottosen, N. S. (1990). "Smeared Crack Analysis using Generalized Fictitious Crack Model," *Journal of the Engineering Mechanics Division*, ASCE, Vol. 116, No. 1, pp. 55-76.

Du, J., Kobayashi, A. S. and Hawkins, N. M. (1990). "Direct FEM Analysis of Concrete Fracture Specimens," *Journal of the Engineering Mechanics Division*, ASCE, Vol. 116, No. 3, pp. 605-619.

Gajer, G. and Dux, P. F. (1990). "Crack Band Based Model for FEM Analysis of Concrete Structures," *Journal of the Structural Division*, ASCE, Vol. 116, No. 6, pp. 1696-1714.

Gopalaratnam, V. S. and Shah, S. P. (1985). "Softening Response of Plain Concrete in Direct Tension," *ACI Journal*, No. 3, pp. 310-323.

Hillerborg, A., Modeer, M. and Petersson, P. E. (1976). "Analysis of Crack Formulation and Crack Growth in Concrete by means of Fracture Mechanics and Finite Elements," *Cement and Concrete Research*, Vol. 6, pp. 773-782.

Hofstetter, G., Simo, J. C. and Tayor, R. L. (1993). "A Modified Cap Model: Closest Point Solution Algorithms," *Computers and Structures*, Vol. 46, No. 2, pp. 203-214.

Ju, J. W. (1989). "On Energy-based Coupled Elastoplastic Damage Theories: Constitutive Modeling and Computational Aspects," *International Journal of Solids and Structures*, Vol. 25, No. 7, pp. 803-833.

Karsan, I. D. and Jirsa, J. O. (1969). "Behavior of Concrete under Compressive Loadings," *Journal of the Structural Division*, ASCE, Vol. 95, No. ST12, pp. 6935-2563.

Lubliner, J., Oliver, J., Oller, S. and Onate, E. (1989). "A Plastic-damage Model for Concrete," *International Journal of Solids and Structures*, Vol. 25, No. 3, pp. 299-326.

Martha L. F., LLorca, J., Ingraffea, A. R. and Elices, M. (1992). "Numerical Simulation of Crack Initiation and Propagation in an Arch Dam," *Dam Engineering*, Vol. 2, Issue 3, 193-213.

Oliver, J. (1989). "A Consistent Characteristic Length of Smeared Cracking Models," *International Journal for Numerical Methods in Engineering*, Vol. 28, pp. 461-474.

Oller, S., Onate, E., Oliver, J. and Lubliner, J. (1990). "Finite Element Nonlinear Analysis of Concrete Structures using a Plastic-damage Model," *Engineering Fracture Mechanics*, Vol. 35, No. 1/2/3, pp. 219-231.

Ortiz, M. and Popov, E. P. (1985). "Accuracy and Stability of Integration Algorithms for Elastoplastic Constitutive Relations," *International Journal for Numerical Methods in Engineering*, Vol. 21, pp. 1561-1567.

Pramono, E. and Willam, K. (1989). "Fracture Energy-based Plasticity Formulation of Plain Concrete," *Journal of the Engineering Mechanics Division*, ASCE, Vol. 115, No. 6, pp. 1183-1203.

Reinhardt, H. W. (1984). "Fracture Mechanics of an Elastic Softening Material like Concrete," *Heron*, Vol. 29, No. 2, pp. 1-42.

Rots, J. G. (1988). "*Computational Modeling of Concrete Fracture*," Dissertation, Department of Civil Engineering, Delft University of Technology, Delft.

Simo, J. C., Kennedy, J. G. and Govindjee, S. (1988). "Non-smooth Multisurface Plasticity and Viscoplasticity. Loading/Unloading Conditions and Numerical algorithms," *International Journal for Numerical Methods in Engineering*, Vol. 26, pp. 2161-2185.

Simo, J. C. and Taylor, R. L. (1985). "Consistent Tangent Operators for Rate-independent Elastoplasticity," *Computer Methods in Applied Mechanics and Engineering*, Vol. 48, pp. 101-118.

Simo, J. C. and Taylor, R. L. (1986). "A Return Mapping Algorithm for Plane Stress Elastoplasticity," *International Journal for Numerical Methods in Engineering*, Vol. 22, pp. 649-670.

Strang, G. (1980). *Linear Algebra and Its Applications*, 2nd ed., Academic Press, NY.

Taylor, R. L. (1992). "FEAP: A Finite Element Analysis Program for Engineering Workstations," *Report UCB/SEMM-92 (Draft Version)*, Department of Civil Engineering, University of California, Berkeley, CA.

Yamaguchi, E. and Chen, W. -F. (1990) "Cracking Model for Finite Element Analysis of Concrete Materials," *Journal of the Engineering Mechanics Division*, ASCE, Vol. 116, No. 6, pp. 1242-1260.

Yazdani, S. and Schreyer, H. L. (1990). "Combined Plasticity and Damage Mechanics Model for Plain Concrete," *Journal of the Engineering Mechanics Division*, ASCE, Vol. 116, No. 7, pp. 1435-1450.

Zienkiewicz, O. C. and Taylor, R. L. (1991). *The Finite Element Method*, 4th ed., Vol. 2, McGraw-Hill, NY.